An experimental and kinetic modeling study of the pyrolysis and oxidation of n-C_3—C_5 aldehydes in shock tubes

Matteo Pelucchi [a,*], Kieran P. Somers [b], Kenji Yasunaga [c], Ultan Burke [b], Alessio Frassoldati [a], Eliseo Ranzi [a], Henry J. Curran [b], Tiziano Faravelli [a]

[a] *Dipartimento di Chimica, Materiali ed Ingegneria Chimica "G. Natta" Politecnico di Milano, Piazza Leonardo da Vinci 32, 20133 Milano, Italy*
[b] *Combustion Chemistry Centre, National University of Ireland, Galway, University Road, Galway, Ireland*
[c] *Department of Applied Chemistry, National Defense Academy, Hashirimizu 1-10-20, Yokosuka 239-8686, Japan*

Received 21 March 2014
Received in revised form 30 May 2014
Accepted 31 July 2014
Available online 24 August 2014

1. Introduction

The depletion of fossil fuel reserves and the stringent targets for air pollution reduction have largely increased the focus on gaseous, liquid and solid biofuels as a sustainable source of energy for transport, domestic and industrial applications. Biomasses can be used to produce either liquid or gaseous biofuels for transportation purposes (hydrogen, methane, ethanol and long chain alcohol, dimethyl ether, diesel) through different processes such as Biomass-To-Liquid (BTL) or as a side product of Gas-To-Liquid (GTL) processes in Fischer–Tropsch synthesis. Similarly, municipal solid waste (MSW), agricultural and forest residues can also be converted to feedstock for energy production through gasification or combustion, followed by conventional power generation cycles.

Within this scenario, low and high molecular weight aldehydes are known to be toxic, some of them carcinogenic, and precursors of free radicals leading to the formation of ozone and urban smog

* Corresponding author.
E-mail address: matteo.pelucchi@polimi.it (M. Pelucchi).

[1]. C_4 and C_5 aldehydes belong to the class of non-regulated pollutants and they are classified as mobile source air toxic (MSAT) compounds. Recent fundamental studies of biofuel combustion have addressed the strong belief that long-chain alcohols (propanol, butanol, pentanol and related isomers) are likely to be used as an alternative to conventional gasoline (*n*-butanol and *iso*-pentanol mainly) either as additives in order to reduce pollution in terms of PAH, particulates and soot formation. Fundamental studies on the oxidation of alcohols identified the presence of aldehydes as intermediate products derived from radical as well as molecular dehydrogenation reactions [2–15].

Aldehydes are products of partial or incomplete combustion and they are released into the atmosphere from conventional spark ignition (SI) gasoline and compression ignition (CI) diesel engines, and also from biomass gasification or aerobic treatments [16]. Grosjean et al. [17] studied carbonyl emissions from light-duty and heavy-duty vehicles on a motorway tunnel, detecting emis-sions of saturated, unsaturated and aromatic aldehydes. Zervas [18] analyzed the exhaust gases from a diesel engine recording high emission of carbonyl compounds, particularly when synthetic fuels were tested compared to a commercial fuel. Karavalakis et al. [19] highlighted how the use of a Euro4 diesel engine increases the emissions (aldehydes and ketones) compared to a Euro3 engine identifying linear aldehydes from formaldehyde up to C_5—C_6 and aromatic aldehydes. De Abrantes and co-workers focused on formaldehyde and acetaldehyde emissions from diesel engines [20], highlighting higher concentrations than those observed in spark ignition engines. Gasoline and diesel engine emissions of aldehydes were also compared by Roy [21] through high performance liquid chromatography. Significant and comparable amounts of formaldehyde, acetaldehyde and propanal were detected from SI and CI engines investigating different injection technologies. Schauer [22] measured the emissions of aldehydes from a gasoline-powered vehicle, detecting concentrations in the order of those measured for diesel engines. Other works in recent years focused on the influence of diesel–biodiesel blended fuels on carbonyl emissions, agreeing that alternative fuel blending increases the release of aldehydes and that the engine technology influences the phenomena as much as the kind of fuel blend itself [23–27].

From a pure chemical kinetics perspective aldehydes are primary stable intermediate products of biofuel oxidation and pyrolysis, influencing reaction pathways and important combustion properties [28]. Therefore their combustion behavior is non-negligible with respect to designing more efficient and environmentally friendly combustion systems. For all of these reasons, the understanding of combustion kinetics of aldehydes and furthermore a deeper understanding of the reactivity of the carbonyl side of the molecule (R—CH═O) under combustion or pyrolytic conditions, play a crucial role in the capability of kinetic mechanisms to better predict pollutant release from both conventional and renewable fuels.

Since the pioneering work of Dean and co-workers [29] and of Hochgreb and Dryer [30], several kinetic studies on the pyrolysis and oxidation of formaldehyde at low- and high-temperature were undertaken [31–38].

Similarly, acetaldehyde oxidation has been described in detail by different authors. Dating back to the early 1970s Halstead et al. [39] discussed cool flames phenomena and low-temperature oxidation. Oscillatory ignitions in the low-temperature regime were studied in the early 1980s by Gray and co-workers [40], and in the 1990s by Cavanagh et al. [41] and by Di Maio et al.[42]. Kaiser et al. proposed a model to describe the negative tem-perature coefficient (NTC) behavior of acetaldehyde [43]. The high-temperature oxidation of acetaldehyde was investigated by Dagaut et al. [44] in a jet-stirred reactor and in a shock tube, while Hidaka and co-workers studied its pyrolysis in a single-pulse shock tube [45], and Yasunaga et al. [46] suggested a mechanism describing the oxidation and pyrolysis for the high-temperature regime.

Da Silva and Bozzelli [47] calculated the enthalpies of formation of C_2 to C_7 *n*-aldehydes through quantum chemical calculations and determined bond dissociation energies (BDE) for all C—C and C—H bonds in the molecules. Their study revealed that the R—CH_2 CH═O bond is the weakest bond in all the aldehydes larger than acetaldehyde, due to the formation of the resonantly stabilized vinoxy radical. Kaiser [48] developed a chemical kinetic model to describe propanal oxidation in the temperature range 400–700 K. An experimental and modeling study at higher temperatures was carried out by Lifshitz and co-workers [49]. They investigated the thermal decomposition of propanal in a single pulse shock-tube under pyrolysis conditions. A sub-mechanism of 52 elementary reaction steps and 22 species was developed, and the kinetic analysis emphasized the importance of unimolecular initiation reactions involving a C—C bond breaking in predicting the intermediate and product species. Furthermore, the species profile predictions were found to be sensitive to the ratio between abstraction by ethyl radical on the fuel molecule and ethyl radical decomposition to form ethylene and a hydrogen atom. Kasper et al.[50] studied the combustion chemistry of propanal in a stoichiom-etric flame at low pressures with molecular beam mass spectrom-etry, highlighting, under the investigated conditions, the importance of alkyl radical addition to the fuel molecule and the need of more detailed kinetic studies to assess the relative impor-tance of available reaction pathways. Akih-Kumgeh and Bergthor-son [51] studied the ignition of propanal in a shock tube and developed a mechanisms underlining the importance of the initia-tion reaction forming $\dot{C}_2H_5$ and H $\dot{C}$O and the H-atom abstraction reactions from the alpha-carbonyl site in predicting ignition delay times. Laminar flame speeds were measured by Veloo et al. [52] together with jet-stirred reactor experiments to quantify reactant, intermediate and product concentrations. A model to describe the low- and high-temperature oxidation of propanal was then devel-oped and validated.

Veloo and co-workers also studied *n*-butanal and *iso*-butanal oxidation in laminar flames and in a jet-stirred reactor proposing a comprehensive mechanism for low- and high-temperature combustion consisting of 244 species and 1198 elementary reaction steps [53]. The authors highlighted the importance of $\dot{C}_3H_5$ radical distribution and other key reaction subsets of the mechanism. An interesting comparison between *n*- and *iso*-butanal and propanal is also shown for flame speed data, with an emphasis on radical species profiles such as H $\dot{C}$O and $\dot{O}$H of high importance in flame propagation phenomena. Davidson and co-workers investigated the ignition behavior of *n*-butanal [54] as part of an update to the Dooley et al. methyl butanoate mechanism [55]. Zhang mea-sured ignition delay times for *n*-butanal [56] and *i*-butanal [57] over a wide range of equivalence ratios, pressures and tempera-tures, and developed kinetic sub-models for both of the C_4 alde-hydes based on a literature review and validated them against the measured data.

To the best of our knowledge, no experimental measurements currently exist for *n*-butanal pyrolysis and *n*-pentanal pyrolysis and oxidation. Furthermore, despite C_3—C_5 aldehydes being included in many hydrocarbon and bio-fuels kinetic models, no studies have specifically addressed to develop and validate an oxi-dation mechanism for *n*-pentanal. There have clearly been signifi-cant efforts focused on understanding the combustion behavior of aldehydes. Yet a consistent and detailed summary of their combustion behavior is still somewhat lacking in the literature.

Two important goals support and justify the present work. Firstly, it provides new experimental data on the pyrolysis and the auto-ignition behavior of C_3—C_5 aldehydes, in order to extend the database available for high-temperature combustion

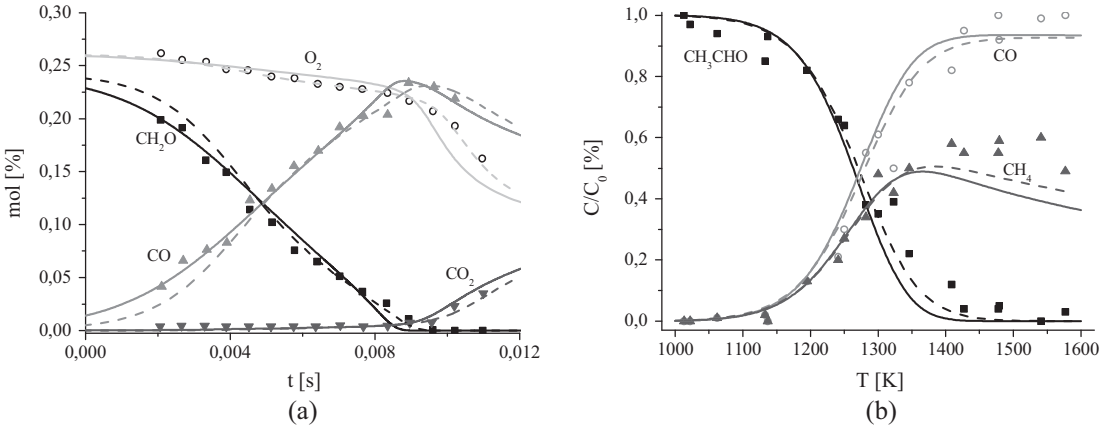

Fig. 1. (a) Oxidation of formaldehyde at 1 atm and 1095 K [31]. (b) Pyrolysis of acetaldehyde at 2 atm and 2 ms residence time [46]. Comparison of experimental data (symbols) and predictions of NUIG (dashed lines) and POLIMI (solid lines) kinetic schemes.

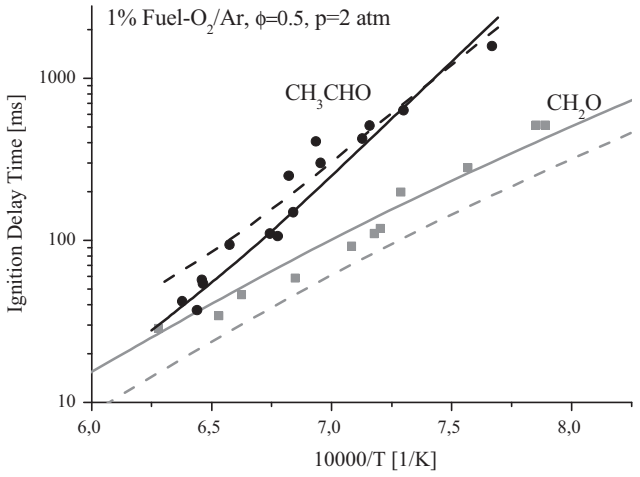

Fig. 2. Ignition delay times of formaldehyde [34] and acetaldehyde [46] oxidation. Comparison of experimental data (symbols) and predictions of NUIG (dashed lines) and POLIMI (solid lines) kinetic schemes.

conditions. Secondly, the experimental data, both from the current study and from the literature, have been used to develop and validate the sub-mechanism of C_3—C_5 aldehydes, with the objective of better characterizing the role of the acyl group. This validation has been performed by coupling a newly developed aldehyde sub-mechanism with the C_0—C_4 mechanism of NUIG [58–63] and the one of POLIMI [64].

The meaning of this joint paper between the two research groups is also a first step toward a unified mechanism. The two C_0—C_4 mechanisms present several differences in the rate con-stants (within their accuracy) and for both of them it is necessary to preserve internal consistency. Internal consistency means that the branching ratio between competitive reactions is more impor-tant than the values of kinetic parameters of single reactions. For this reason, reactions within the C_0—C_4 mechanism (including C_1—C_2 aldehydes) have forced some differences between the implementation of the aldehyde sub-mechanism within the two kinetic frameworks. As a matter of fact, the concentration of $\dot{H}$, $\dot{O}H$ and other radicals are mainly controlled by two different C_0—C_4 mechanisms. More than the same kinetic constants (k) it is important to have the same rate parameters (k *[R]* s-1), that is the reason why there are differences between the two mecha-nisms. The unification process would need to start from the C_0—C_4 mechanism, which is beyond the aim of this study, and would require more time and efforts. Moreover, the POLIMI kinetic mechanism is systematically reduced by using a lumping approach; this is not considered nor applied in the NUIG mechanism.

Both the mechanisms were previously validated for formaldehyde and acetaldehyde. Figure 1 shows a first comparison with experimental data. Figure 1a shows the oxidation of formaldehyde in an atmospheric pressure flow reactor at 1095 K and φ = 1.08 [31], while Fig. 1b shows the high-temperature pyrolysis of acetaldehyde in a shock tube [46]. Figure 2 compares the ignition delay times of formaldehyde [34] and acetaldehyde [46] (1% fuel in oxygen-argon) at lean conditions (φ = 0.5). The higher reactivity of formaldehyde is evident in this figure, mainly at lower temperatures. The apparent activation energies are significantly different, in the order of 40 kcal mol^{-1} for formaldehyde and close to 60 kcal mol^{-1} for acetaldehyde. At temperatures higher than 1600 K, both aldehydes have similar reactivity. These comparisons show that both of the models agree with the experimental data, providing a solid basis for the development of kinetic mechanisms for heavier aldehydes.

2. Experimental approach

Two shock tubes were used in this study, the first one at the National Defense Academy in Japan to study the pyrolysis of aldehydes, the second one, at the National University of Ireland Galway (NUIG), was used to measure ignition delay times of propanal, *n*-butanal and *n*-pentanal at different oxidation conditions.

2.1. Pyrolysis

Pyrolysis experiments were performed in a single-pulse magic-hole type shock tube (SPST) [65–68] at 3% fuel in argon (99.9999% pure, Tokyo Koatsu Yamazaki). Samples of propanal and *n*-pentanal 99.0+% and 97.0+% pure respectively, were supplied by Kanto Chemical Co., Inc., *n*-butanal 98.0+% pure was supplied by Alfa Aesar. The experimental conditions studied are summarized in Table 1.

The shock tube consists of an adjustable driver section 40–140 cm in length, allowing modifications of the heating time, and a test section measuring 3.60 m in length. The two sections are separated by a polyethylene terephthalate (PET) diaphragm which bursts when a needle is dropped. Three pressure transducers are located along the last 30 cm of the test section, shock velocity at the end-wall is determined through linear extrapolation, taking

Table 1
Summary of experimental work carried out in the SPST at the National Defense Academy, Japan.

Aldehyde	Fuel (%)	Ar (%)	T_{range} (K)	p (atm)	t_e (ms)
Propanal	3.0	97.0	1013–1356	1.8 ± 0.3	2.6 ± 0.5
n-Butanal	3.0	97.0	1096–1368	1.9 ± 0.5	1.9 ± 0.5
n-Pentanal	3.0	97.0	972–1372	2.1 ± 0.4	2.3 ± 0.5

shock wave attenuation into account. The Gaseq [69] equilibrium program was used to determine the reflected shock parameters from the known initial temperature, mixture pressure and incident shock velocity *via* the usual one-dimensional equations. The validity of the experimental method used in this study and reiterated in this Section has been also recently proved in the investigation of the pyrolysis of 2,5-dimethylfuran by Somers et al. [70].

The reacted gas mixtures, quenched using the single-pulse method, were extracted into a pre-evacuated vessel (50 cm^3) through a valve near the end-plate. The reacted gas mixtures were analyzed by three serially connected gas chromatographs equipped with thermal conductivity detectors (TCD) [67,68].

Shimadzu GC-8APT with helium as carrier gas, equipped with different columns, was used for the different analysis in the post-shock mixtures:

- A 2 m column packed with Sebaconitrile and heated to 348 K to detect propanal.
- A 2 m column of Porapak Q coupled with a 2 m column of Unibeads 1S to determine C_2 and C_3 hydrocarbons.
- A 2 m column of Molecular Sieve 5A at 323 K to determine methane and CO.

According to Hidaka et al. [66,67], an effective reaction time (t_e) was defined as the time between the heating of the mixture by the reflected shock wave and the time at which the reflected shock pressure had fallen by 20%. Assuming the adiabatic expansion of a non-reactive mixture, the temperature drops by ≈8.5% from its initial value at t_e. Given that the single-pulse shock tube has cooling rates of 6.6×10^5 K s^{-1} [65], it can be assumed that the reaction was frozen at t_e. The validity of the effective heating time and cooling rate was previously tested for N_2O pyrolysis [65].

The uncertainty in the measured concentration of small hydrocarbons in the post-shock mixtures is less than 2%, except for fuels where the estimate uncertainty is less than 8% for propanal and *n*-butanal, and less than 28% for *n*-pentanal. The uncertainty in the reaction time is 5% and in the reflected shock temperature is±1%. Maximum uncertainties in the reflected pressure are±0.5 atm based on the standard deviation (σ) of our experiments, while those in the residence time are ±0.5 ms.

2.2. Ignition delay times

The shock tube based at NUI Galway, a standard type UV Emission Shock Tube (UEST), was previously described in detail by Smith et al. [71] and will be briefly discussed here. It consists of a test section measuring 6.22 m in length with an internal diame-ter of 10.24 cm and a barrel-shaped driver section measuring 53 cm in length. The two sections are separated by a polycarbonate diaphragm which bursts when forced into contact with a cross-shaped cutter due to the pressure differential. Four pressure transducers located along the last half meter of the test section were used to determine the velocity of the incident shock wave. The velocity at the end-plate was determined via linear extrapolation, taking shock wave attenuation into account. The Gaseq [69] equilibrium program was used to determine the reflected shock parameters from the known initial temperature, mixture pressure and incident shock velocity *via* the usual one-dimensional equations. Given the large diameter of the shock tube facility, the boundary layers have limited effect, thus the test conditions are closely predicted by the one-dimensional equations [72].

The pressure at the end-plate was recorded using a pressure transducer (Kistler, model 603B). Light emission at 431 nm from excited $CH^\star$ radical was detected through a fused silica window embedded in the end-plate using a photo-detector (Thorlabs Inc. PDA55-EC) and a narrow band-pass filter centered at 430 nm, with a full width half-maximum of 10 nm. The ignition delay time was defined as the time interval between the rise in pressure due to the arrival of the shock wave at the end-plate and the extrapolation of the maximum slope of $CH^\star$ emission to the zero signal level as reported in Fig. 3.

Propanal (97.0+% pure) was supplied by Sigma–Aldrich while *n*-butanal (99.0%) and *n*-pentanal (97.0+%) were supplied by TCI Europe. Fuels were degassed before being introduced into the mixing tanks by a series of freeze–pump-thaw cycles until no gas was observed to escape from the fuel as the solid thawed. Oxygen (99.5%) and argon (99.998%) were provided by BOC Ltd and were introduced in the mixing tanks through the manifolds from gas cylinders. For each aldehyde, 1% fuel mixtures were prepared at three different equivalence ratios (φ = 0.5, 1.0 and 2.0) using the method of partial pressures and their compositions are provided in Table 2, together with the temperatures and pressures measured for each mixture. We estimate an uncertainty of ±0.10 and ±0.25 atm in the reflected shock pressure, respectively for 1 and 3 atm experiments, based on the standard deviation (σ) of the data. Uncertain-ties of ∼1% are present in the reflected shock temperature. An uncertainty of ∼15% is estimated in the ignition delay time of each experiment due to uncertainties in the condition behind the reflected shock wave. Uncertainties in the mole fractions of reac-tants are minimal (<5%) as high accuracy digital pressure gauges were used in the preparation of the mixture.

3. Kinetic mechanism of aldehydes

3.1. Thermochemistry

The thermodynamic data for the three aldehydes (Fig. 4) and related radicals, were calculated using the THERM program from

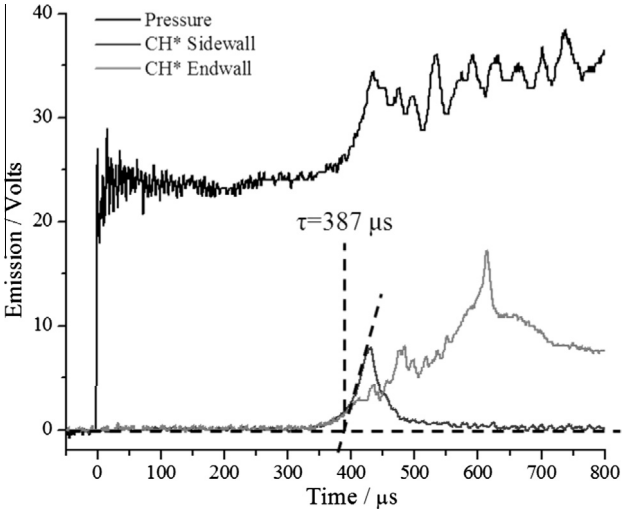

Fig. 3. End-wall pressure trace and $CH^\star$ chemiluminescence measurements with corresponding ignition delay time, 1% *n*-butanal, 5.5% O_2, 93.5% Ar, p = 1.2 atm, T = 1349 K.

Table 2
Summary of experimental work carried out in the low pressure shock tube at the National University of Ireland, Galway.

Fuel	φ	Fuel (%)	O_2 (%)	Ar (%)	T_5 (K)	p (atm)
Propanal	0.5	1	8	91	1136–1405	1.25 ± 0.08
					1170–1336	2.49 ± 0.13
	1	1	4	95	1171–1612	1.22 ± 0.12
					1201–1479	2.75 ± 0.25
	2	1	2	97	1358–1747	1.21 ± 0.09
					1302–1598	2.91 ± 0.30
n-Butanal	0.5	1	11	88	1232–1495	1.10 ± 0.06
					1224–1424	3.14 ± 0.11
	1	1	5.5	93.5	1303–1547	1.20 ± 0.13
					1271–1475	3.23 ± 0.16
	2	1	2.75	96.25	1376–1740	1.07 ± 0.05
					1321–1610	2.84 ± 0.17
n-Pentanal	0.5	1	14	85	1211–1447	0.98 ± 0.05
					1167–1338	3.01 ± 0.33
	1	1	7	92	1226–1538	1.06 ± 0.05
					1181–1481	2.89 ± 0.15
	2	1	3.5	95.5	1363–1847	1.08 ± 0.07
					1238–1592	3.16 ± 0.11

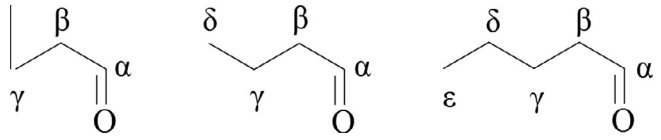

Fig. 4. Propanal, *n*-butanal and *n*-pentanal chemical structure and named carbon sites.

Ritter and Bozzelli [73], based on group additivity methods developed by Benson [75] and further optimized by Burke [61] at NUIG. The computed values of enthalpies, entropies of formation and heat capacities for aldehydes and primary radicals are shown in Table 3, together with enthalpies of formation computed by da Silva and Bozzelli [47], and the nomenclature used in this study. Good agreement between the group additivity rules and the theoretical computations is shown in Table 3, with maximum deviations being within 1.5–2.0 kcal mol^{-1} for the enthalpies of formation. The bond dissociation energies (BDE) for the three aldehydes will be analyzed in the next paragraph when discussing chain initiation reactions.

3.2. Primary reactions of aldehydes

Figs. 5–7 show simplified primary chain initiation and propagation reactions of the three aldehydes, in terms of initiation, H-atom abstraction, and radical decomposition reactions. The chain initiation reactions occur *via* unimolecular decompositions with a C—C bond cleavage, forming an alkyl radical and an oxygenated radical (H $\dot{C}O$, $\dot{C}H_2CHO$, $\dot{C}_2H_4CHO$-2, $\dot{C}_3H_6CHO$-3). In flame conditions, the chain initiation and the reverse recombination reactions involving the C—H bonds can become significant. H-atom abstraction reactions are reported in their general form with $\dot{R}$ being the generic H-atom abstracting radical. These reactions lead to three, four and five primary fuel radicals, respectively, for propanal, *n*-butanal and *n*-pentanal. Radical decomposition reactions proceed to form either an alkene and an oxygenated radical or an unsaturated oxy-genated species (CO, ketene, acrolein, methylketene, or 1-butenal) and a small alkyl radical. For instance, the α-radical derived from the C_n aldehyde could, in principle, decompose via β-scission to form either ketene and a C_{n-2} alkyl radical or, more likely, CO and a C_{n-1} alkyl radical. Radicals can also isomerize mainly to form the thermodynamically favored α-radical. For the sake of clarity, isomerization pathways are not reported in Figs. 5–7.

3.2.1. Unimolecular decomposition reactions

A three-frequency version of Quantum-Rice–Ramsperger–Kassel theory (QRRK/MSC) [75–77] was used to calculate the temperature and pressure dependency of unimolecular decomposition reactions involving the three aldehydes. Collisional stabilization was calculated using a modified strong collision approximation. The high-pressure limiting rate constants were calculated through microscopic reversibility using estimates for radical–radical recombination reactions. Table 4 shows the resulting BDE compared to those evaluated by da Silva and Bozzelli [47]. The C_β—C_γ is the weakest bond, as would be expected from the proximity to the electron withdrawing carbonyl group, followed by C_α—C_β. The weakest C—H bond is the C_α—H, followed by C_β—H. Once again group additivity methods show good agreement with theoretical computations.

Table 5 reports the high-pressure limit rate parameters of initiation reactions in the non-Arrhenius form $A\,T^n \exp[-E_a/RT]$, where A is the frequency factor, E_a is the activation energy, and R is the gas constant. Units are: cm^3, mol, s, cal, K. Relative branching ratios at four different temperatures of 1000, 1500, 2000 and 2500 K are also shown. Whilst for propanal the decomposition is mainly initiated by C_α—C_β breaking throughout the temperature range explored, for T < 1500 K, the chain initiation for *n*-butanal and *n*-pentanal mainly occurs via the breakage of the C_β—C_γ bond to form the $\dot{C}H_2CHO$ radical. As already mentioned, the C_α—H bond cleavage contributes to the chain initiation only at high temperatures, and even then, it is still negligible due to its high activation energy. In order to support the QRRK/MSC approach, a direct compari-son between QRRK/MSC and QC/RRKM/ME approaches for prop-anal dominant unimolecular decomposition channels (C_α—C_β and C_β—C_γ breaking) is presented in Fig. 8. A complete description of the quantum chemical, RRKM/ME and QRRK/MSC methods and results is provided in Supplementary Material for brevity in the main text. Quantum chemical calculations were carried out using the Gaussian 09 application [78], with the B3LYP functional [79,80] and the CBSB7 basis set used to optimize geometries, to determine frequencies (scaled by 0.99), and to carry out relaxed scans of internal rotors for use in a 1-D hindered rotor approximation. The average energy transferred in a deactivating collision was estimated as $\langle \Delta E_d \rangle(T) = 200(T/300)^{0.85}$ cm^{-1} which is in line with recent RRKM/ME calculations carried out on the potential energy surfaces of propoxy [81] and butoxy [82] radicals. All calculations were carried out in an argon bath gas with Lennard-Jones parameters of σ = 3.53 Å and ε/k_B = 162 K assumed. Lennard-Jones

Table 3
Thermochemical data and nomenclature of aldehydes and related primary radicals (*group additivity).

Aldehyde and radical site	Name	$\Delta H°_f$ (298.15 K) [47] (kcal mol^{-1})	$\Delta H°_f$ (298.15 K)* (kcal mol^{-1})	$S°$(298.15 K)* (kcal mol^{-1})	C_p (cal mol^{-1} K^{-1})*				
					300 K	500 K	800 K	1000 K	1500 K
Propanal	C_2H_5CHO	−45.18	−45.35	72.86	19.38	26.94	36.90	42.12	49.83
α	$C_2H_5\dot{C}O$	−8.00	−8.45	73.98	18.55	24.98	33.74	38.39	45.19
β	$\dot{C}_2H_4CHO$-1	−7.10	−5.55	70.49	18.02	25.21	34.24	39.01	46.33
γ	$\dot{C}_2H_4CHO$-2	5.10	3.73	76.20	18.85	25.19	33.53	38.03	44.79
n-Butanal	*n*-C_3H_7CHO	−50.00	−50.31	82.28	24.82	35.26	48.21	54.29	64.57
α	*n*-$C_3H_7\dot{C}O$	−13.00	−13.41	83.40	23.99	33.30	45.05	50.56	59.93
β	$\dot{C}_3H_6CHO$-1	−11.50	−10.51	79.91	23.46	33.53	45.55	51.18	61.07
γ	$\dot{C}_3H_6CHO$-2	−2.50	−4.48	86.29	23.29	32.26	44.04	49.65	59.28
δ	$\dot{C}_3H_6CHO$-3	0.10	−1.23	85.62	24.29	33.51	44.84	50.20	59.53
n-Pentanal	*n*-C_4H_9CHO	−54.61	−55.27	91.70	30.26	43.58	59.52	66.46	79.31
α	*n*-$C_4H_9\dot{C}O$	−18.30	−18.37	92.82	29.43	41.62	56.36	62.73	74.67
β	$\dot{C}_4H_8CHO$-1	−17.20	−15.47	89.33	28.90	41.85	56.86	63.35	75.81
γ	$\dot{C}_4H_8CHO$-2	−8.10	−9.44	95.71	28.73	40.58	55.35	61.82	74.02
δ	$\dot{C}_4H_8CHO$-3	−7.60	−9.44	95.71	28.73	40.58	55.35	61.82	74.02
ε	$\dot{C}_4H_8CHO$-4	−5.20	−6.19	95.04	29.73	41.83	56.15	62.37	74.27

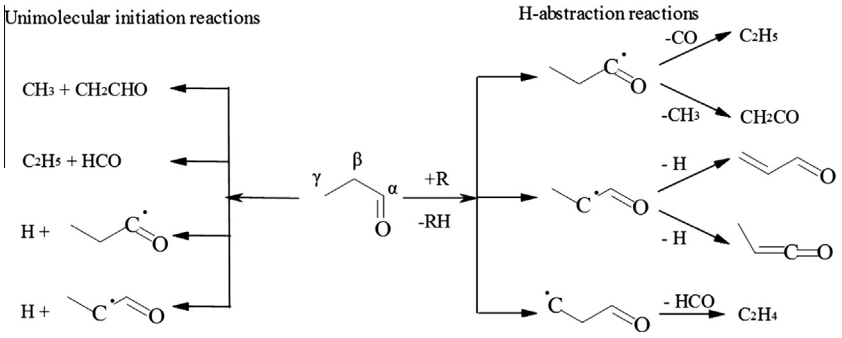

Fig. 5. Primary decomposition reactions of propanal.

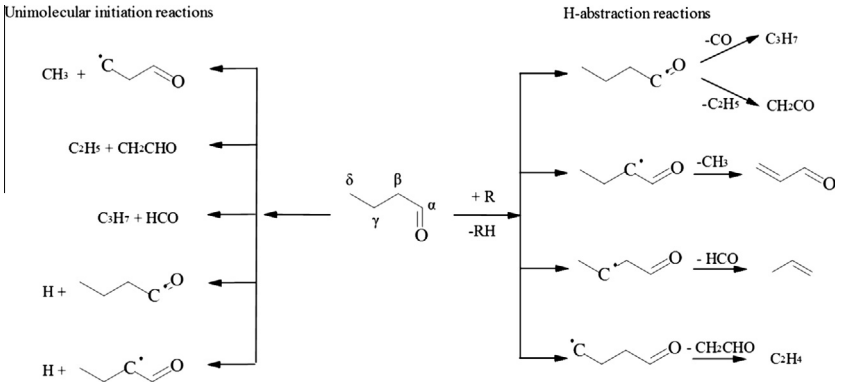

Fig. 6. Primary decomposition reactions of *n*-butanal.

parameters for all three aldehydes were estimated from their critical constants [83] and the empirical correlations recommended by Kee and co-workers [84]. RRKM/ME computations for the two dominant unimolecular fission reactions were carried out using the MultiWell code [85,86] using the ILT method to computed $k(E)$. Identical high-pressure limiting rate constants and energy transfer parameters were assumed in QRRK/MSC and RRKM/ME computations. QRRK/MSC results are shown to agree with the more rigorous RRKM/ME computations to within 80% under the conditions tested. Both approaches highlight that above 1 atm, fall-off in the primary unimolecular decomposition pathways of propanal is limited below 1500 K. Above this temperature, the kinetic model showed little sensitivity to the inclusion of fall-off. As part of *this work*, the QRRK/MSC approach was also validated against RRKM/ME and experimental measurements of analogous alkane decompositions from Oehlschlaeger et al. [87,88] where a factor of 2–3 agreement in $k(T,p)$ was observed when the QRRK/MSC and RRKM/ME/experimental recommendations were compared. Detailed results together with a detailed quantification of the fall-off behavior of aldehydes are reported in the Supplementary Material attached to this study. The above results re-enforce the applicability of the QRRK/MSC method as a means to include

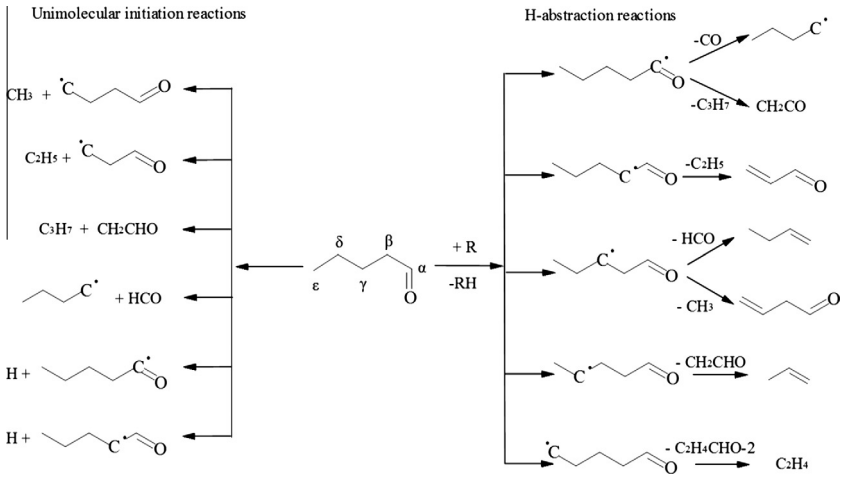

Fig. 7. Primary decomposition reactions of *n*-pentanal.

Table 4
Calculated bond dissociation energies (kcal mol^{-1}) of C—C and C—H bonds and comparison to *ab initio* computed values by da Silva and Bozzelli [47].

Bond	Propanal		*n*-Butanal		*n*-Pentanal	
	This work	[47]	This work	[47]	This work	[47]
C_α—C_β	84.4	83.8	84.6	84.1	84.5	83.4
C_β—C_γ	83.5	83.7	82.3	82.5	82.5	82.3
C_γ—C_δ			89.1	90.1	87.9	88.5
C_δ—C_ε					89.1	89.4
C_α—H	89.0	89.3	89.0	89.1	89.0	88.8
C_β—H	91.9	90.2	91.9	90.6	91.9	89.5

a cost-effective assessment of the influence of fall-off in the kinetic modeling of our high-temperature experiments.

3.2.2. H-abstraction reactions

Rate constant for abstractions of the acyl H-atom at the α position were estimated by analogy with the same site in formaldehyde and acetaldehyde. The presence of the H—C=O groups leads to the formation of resonantly stabilized radicals and the reactivity of the H-atoms in the β site is slightly enhanced with respect to secondary H-atoms in alkanes. This fact is also evident observing the enthalpy of formation in Table 3 and it is further supported by the kinetic study of 3-pentanone oxidation by Serinyel et al. [89]. Rate constants for abstractions from the remaining secondary and primary H-atoms were adopted according to their values used for *n*-alkanes [90,91].

Rate constants for this class of reactions need to be defined for all the H-atom abstracting radicals. To maintain an internal consistency inside NUIG and POLIMI mechanisms, rate parameters for H-atom abstraction reactions are defined in two different ways, but still within their kinetic uncertainty, as will be discussed in Sections 4.1 and 4.2.

3.2.3. Radical decomposition reactions

Arrhenius parameters for the decomposition of α-radicals to form CO were taken from the evaluation by Simmie [92] for 1-oxo-butyl radical (n-$C_3H_7\dot{C}O$) decomposition to *n*-propyl radical and CO. β-scission to form ketene and C_{n-2} alkyl radical has also been included in the kinetic scheme, based on the following

Table 5
High-pressure limit rate parameters of initiation reactions and relative branching ratios at different temperatures [units are: cm^3, mol, s, cal].

Reactions	k_i (s^{-1})			Branching ratios (%)			
	A_i	n_i	E_{ai}	1000 K	1500 K	2000 K	2500 K
Propanal							
$C_2H_5CHO \leftrightarrow \dot{C}H_3+\dot{C}H_2CHO$	1.16E+25	−2.80	85718	32.9	31.4	29.7	27.1
$C_2H_5CHO \leftrightarrow \dot{C}_2H_5 + H\dot{C}O$	1.34E+26	−3.00	86406	66.5	65.6	62.1	56.0
$C_2H_5CHO \leftrightarrow C_2H_5\dot{C}O+\dot{H}$	9.42E+16	−0.43	89167	0.6	2.7	6.6	12.2
$C_2H_5CHO \leftrightarrow \dot{C}_2H_4CHO\text{-}1+\dot{H}$	1.22E+15	−0.08	91694	0.0	0.2	0.7	1.5
$C_2H_5CHO \leftrightarrow \dot{C}_2H_4CHO\text{-}2+\dot{H}$	5.80E+17	−0.52	101476	0.0	0.1	0.9	3.2
n-Butanal							
n-$C_3H_7CHO \leftrightarrow \dot{C}H_3+\dot{C}_2H_4CHO\text{-}2$	1.09E+24	−2.25	90369	4.1	14.4	26.2	36.2
n-$C_3H_7CHO \leftrightarrow \dot{C}_2H_5+\dot{C}H_2CHO$	5.04E+27	−3.50	84479	67.3	52.3	40.5	31.5
n-$C_3H_7CHO \leftrightarrow n\dot{C}_3H_7 + H\dot{C}O$	7.49E+27	−3.51	86758	28.4	32.1	30.0	26.1
n-$C_3H_7CHO \leftrightarrow$ n-$C_3H_7\dot{C}O+\dot{H}$	2.72E+17	−0.58	88995	0.2	1.1	3.0	5.5
n-$C_3H_7CHO \leftrightarrow \dot{C}_3H_6CHO\text{-}1+\dot{H}$	3.62E+15	−0.23	91529	0.0	0.1	0.3	0.7
n-Pentanal							
n-$C_4H_9CHO \leftrightarrow \dot{C}H_3+\dot{C}_3H_6CHO\text{-}3$	1.18E+22	−1.61	90120	3.3	9.9	16.5	22.0
n-$C_4H_9CHO \leftrightarrow \dot{C}_2H_5+\dot{C}_2H_4CHO\text{-}2$	2.84E+24	−2.24	89004	17.1	33.4	42.1	45.8
n-$C_4H_9CHO \leftrightarrow n\dot{C}_3H_7+\dot{C}H_2CHO$	1.70E+27	−3.31	84704	57.9	35.6	23.1	16.0
n-$C_4H_9CHO \leftrightarrow n\dot{C}_4H_9 + H\dot{C}O$	1.20E+26	−2.94	86380	21.6	20.4	16.8	13.7
n-$C_4H_9CHO \leftrightarrow n$-$C_4H_9\dot{C}O+\dot{H}$	1.64E+17	−0.50	89262	0.1	0.6	1.3	2.1
n-$C_4H_9CHO \leftrightarrow \dot{C}_4H_8CHO\text{-}1+\dot{H}$	4.06E+14	0.11	91691	0.0	0.1	0.2	0.4

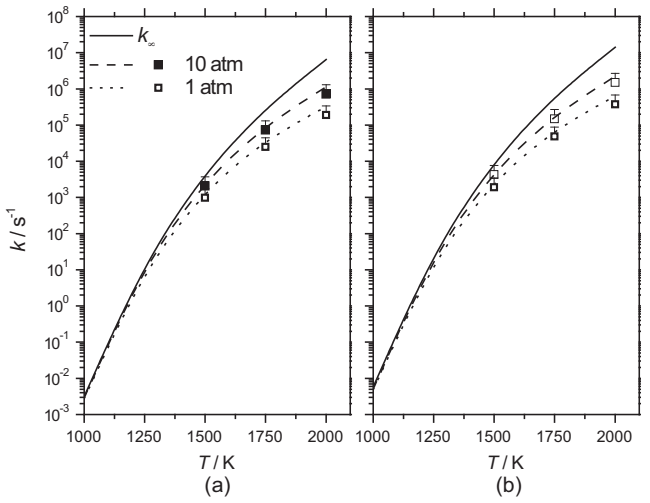

Fig. 8. Comparison of RRKM/ME (symbols) and QRRK/MSC (dashed lines) derived $k(T,p)$ for propanal thermal decomposition to (a) CH_3 and CH_2CHO and (b) $HCO + C_2H_5$. 80% uncertainty bars illustrate the agreement between the two methods.

rationale. Methyl radical addition to ketene to form 1-oxo-propyl radical ($C_2H_5\dot{C}O$) was taken as a reference and the kinetic parameters were estimated by analogy with methyl radical addition to propylene [93]. Rate constants for the analogous β-scission of 1-oxo-butyl and 1-oxo-pentyl radical (n-$C_4H_9\dot{C}O$) were based on the *ab initio* calculations of Huynh and Violi [94].

For the β-radical decomposition to form acrolein (C_2H_3CHO, 1-propenal) and an alkyl radical the recommended values of Curran [93] for the reverse addition reaction are used. Rate parameters for the dehydrogenation reactions of $\dot{C}_2H_4CHO$-1 radical to form acrolein or methylketene are derived from the kinetic values of the reverse Ḣ-atom addition to propylene to give *iso*-propyl radical. Methyl and ethyl radical addition to propylene to form the secondary radicals were used to derive the corresponding decomposition of β-radicals of *n*-butanal and *n*-pentanal, forming acrolein and a methyl or an ethyl radical, respectively.

β-Scission of γ-radicals to produce formyl radicals and alkenes, were based on computations of *n*-butanal radical decomposition by Huynh and Violi [94]. Rate constant for the decomposition of propanal γ-radical to form HĊO and ethylene, was taken from HĊO addition to propylene [94] accounting for the symmetry effect. The γ-radical of pentanal ($\dot{C}_4H_8CHO$-2) can also form a methyl radical and 1-butenal. Similarly to the estimate for methyl radical addition to acrolein in butanal, methyl radical addition to propylene was used as a reference reaction [93].

Again, the *n*-butanal calculations by Simmie [92] were adopted for the decomposition of δ-radicals to form ethylene (or propylene) and $\dot{C}H_2CHO$ radical.

Finally, the decomposition of the ε-radical ($\dot{C}_4H_8CHO$-4) of *n*-pentanal to produce ethylene and the γ-radical of propanal were based on analogy with the addition of alkyl radicals to ethylene, as suggested by Orme et al. [90].

Table 6 summarizes the decomposition reactions and relating kinetic parameters, together with literature references.

3.2.4. Radical isomerization reactions

Radical isomerization reactions, i.e. internal H-atom shift through 3-, 4-, 5- and 6-membered ring intermediates, were also considered. Reaction rate constants were estimated according general rules [95–97]. The activation energy was estimated through Evans–Polanyi correlations accounting for reaction enthalpy of the H-atom shift reaction and the ring strain energy associated with ring formation in the transition state. Frequency factors were estimated on the basis of hindered rotor effects. As the ring intermediate gets bigger, the reactions become energetically more favored due to lower ring strain energies, but conversely are entropically inhibited due to the loss of internal rotors. Isomerization reactions of the different radicals and kinetic parameters are reported in Table 6.

Table 6
Rate constant parameters of decomposition and isomerization reactions of aldehydes radicals [units are: cm^3, mol, s, cal] and references.

Reaction				
Propanal radicals	A	n	Ea	[Ref.]
$\dot{C}_2H_4CHO$-2 ⇔ $C_2H_5\dot{C}O$	3.80E+10	0.67	30200.0	[95]
$\dot{C}_2H_4CHO$-1 ⇔ $C_2H_5\dot{C}O$	3.56E+10	0.88	37300.0	[95]
$C_2H_5\dot{C}O$ ⇔ CO + $\dot{C}_2H_5$	5.78E+14	0.00	16843.5	[92][a]
$\dot{C}H_3$ + CH_2CO ⇔ $C_2H_5\dot{C}O$	1.76E+04	2.48	6130.0	[93][a]
Ḣ + C_2H_3CHO ⇔ $\dot{C}_2H_4CHO$-1	4.24E+11	0.51	1230.0	[93][a]
Ḣ + CH_3CHCO ⇔ $\dot{C}_2H_4CHO$-1	4.24E+11	0.51	1230.0	[93][a]
HĊO + C_2H_4 ⇔ $\dot{C}_2H_4CHO$-2	2.56E+02	2.89	6728.4	[94][a]
n-Butanal radicals				
$\dot{C}_3H_6CHO$-3 ⇔ $nC_3H_7\dot{C}O$	7.73E+11	0.00	15464.4	[95]
$\dot{C}_3H_6CHO$-2 ⇔ $nC_3H_7\dot{C}O$	3.80E+10	0.67	32100.0	[95]
$\dot{C}_3H_6CHO$-1 ⇔ $nC_3H_7\dot{C}O$	3.56E+10	0.88	37300.0	[95]
$nC_3H_7\dot{C}O$ ⇔ $n\dot{C}_3H_7$ + CO	5.78E+14	0.00	16843.5	[92]
$\dot{C}_2H_5$ + CH_2CO ⇔ $nC_3H_7\dot{C}O$	3.33E+02	2.73	13953.9	[94]
$\dot{C}H_3$ + C_2H_3CHO ⇔ $\dot{C}_3H_6CHO$-1	1.76E+04	2.48	6130.0	[93][a]
HĊO + C_3H_6 ⇔ $\dot{C}_3H_6CHO$-2	1.28E+02	2.89	6728.4	[94]
$\dot{C}_3H_6CHO$-3 ⇔ $\dot{C}H_2CHO$ + C_2H_4	3.95E+13	0.00	22316.3	[92]
n-Pentanal radicals				
$\dot{C}_4H_8CHO$-4 ⇔ $nC_4H_9\dot{C}O$	3.67E+12	−0.60	7090.0	[95]
$\dot{C}_4H_8CHO$-3 ⇔ $nC_4H_9\dot{C}O$	7.85E+11	−0.12	16800.0	[95]
$\dot{C}_4H_8CHO$-2 ⇔ $nC_4H_9\dot{C}O$	3.80E+10	0.67	32100.0	[95]
$\dot{C}_4H_8CHO$-1 ⇔ $nC_4H_9\dot{C}O$	3.56E+10	0.88	37300.0	[95]
$nC_4H_9\dot{C}O$ ⇔ $p\dot{C}_4H_9$ + CO	5.78E+14	0.00	16843.5	[92][a]
$n\dot{C}_3H_7$ + CH_2CO ⇔ $nC_4H_9\dot{C}O$	3.33E+02	2.73	13953.9	[94][a]
$\dot{C}_2H_5$ + C_2H_3CHO ⇔ $\dot{C}_4H_8CHO$-1	8.80E+03	2.48	6130.0	[93][a]
HĊO + C_4H_8-1 ⇔ $\dot{C}_4H_8CHO$-2	1.28E+02	2.89	6728.4	[94]
$\dot{C}H_3$ + C_3H_5CHO ⇔ $\dot{C}_4H_8CHO$-2	1.76E+04	2.48	6130.0	[93][a]
$\dot{C}H_2CHO$ + C_3H_6 ⇔ $\dot{C}_4H_8CHO$-3	1.88E+02	3.11	3660.0	[92][a]
$\dot{C}_2H_4CHO$-2 + C_2H_4 ⇔ $\dot{C}_4H_8CHO$-4	1.32E+04	2.48	6130.0	[90][a]

[a] Extended analogy as discussed in this paper.

Due to their possible competing effect, a comparison of decomposition and isomerization rate constants of each radical is relevant. Figure 9 shows this comparison for *n*-pentanal radicals in the temperature range 1000–2500 K. Figure 9d shows the 1–5 isomerization reaction of the ε-radical, occurring through the energetically favored six membered ring intermediate, which prevails over the decomposition channel at temperatures lower than ∼1430 K. The remaining figures show that generally, the decompo-sition paths dominate. Moreover, Fig. 9b shows that for *n*-pentanal γ-radical ($\dot{C}_4H_8CHO$-2) the decomposition reaction to form 3-butenal and a methyl radical prevails over the alternate channel generating 1-butene and a formyl radical. Decomposition of the α-radical (1-oxo-pentyl radical, n-$C_4H_9\dot{C}O$) to form CO and an *n*-butyl radical largely prevails over the 1–5 isomerization reaction in the complete range of temperature. For this reason reaction rate constants for the α-radical are not reported in Fig. 9. A similar analysis for propanal and *n*-butanal radicals is reported in the Supplementary Material.

4. Numerical methods and overall kinetic mechanisms

All numerical simulations were performed using the OpenSMOKE code, which is an upgraded and extended version of the well-tested DSMOKE code. A shock tube is considered a constant

volume batch system where the energy equation is solved, thus accounting for both endothermic and/or exothermic gradients. The conservation equations with proper boundary conditions were discretized by means of conventional finite differencing techniques with non-uniform mesh spacing for the simulation of premixed laminar flames. A mixture-averaged formula was also used to compute multicomponent diffusion coefficients. Further details of the numerical methods are reported elsewhere [98–100].

The computed sensitivity coefficient, S_y, is normalized (s_y) as follows:

$$s_y = \frac{\delta \ln y}{\delta \ln A} = \frac{A}{y}\frac{\delta y}{\delta A} = \frac{A}{y}S_y$$

where y is the species concentration or the ignition delay time and A the generic frequency factor.

The Transport Data Estimator package of the Reaction Mechanism Generator software of Green and co-workers has been used to provide relevant transport properties [70].

4.1. NUIG kinetic mechanism

The aldehyde mechanism was coupled with the NUIG C_0—C_4 sub-mechanism, recently revised and validated as reported in several recent studies [58–63].

H-atom abstraction rates at the β secondary site forming $\dot{C}_nH_{2n}CHO - 1 \quad (n = 2, 3, 4)$ radicals were based on those for secondary H-atom abstractions in ketones. Rate constants for H-abstractions by $\dot{O}H$ and $H\dot{O}_2$ radicals were taken from the *ab initio* calculations for ethylmethyl ketone by Zhou et al. [101] and by Mendes et al. [102] respectively.

Before coupling the aldehyde sub-mechanism with the NUIG kinetic scheme, some modifications were made.

The total initiation rate constant for *n*-butanal has been increased of a factor of 1.5 with respect to the calculated reaction rates previously discussed in Section 3.2.1. This correction factor, well within the kinetic uncertainty, has been also applied to POLIMI mechanism. H-atom abstraction from the α carbonyl site has been decreased by about 20% with respect to the reference abstraction from acetaldehyde. Rate constants for abstraction reactions by $\dot{H}$, $\dot{O}H$, $\dot{C}H_3$ and $H\dot{O}_2$ radicals are listed in the Supplementary Material. Moreover, overall rate constants of H-abstraction by $\dot{O}H$ radical for C_1—C_4 aldehydes were studied in shock tubes very recently by Wang et al. [103], further supporting the kinetic parameters here proposed.

The overall kinetic model, with thermodynamic and transport properties, consisting of 2,011 reactions and 329 species is available as part of the Supplementary Material.

4.2. POLIMI kinetic mechanism

Metathesis reactions are treated according to the systematic approach described by Ranzi et al. [104]. The reactivity of primary and secondary H-atoms are considered to be the same as those for alkanes. Similar to the acyl H-atoms of formaldehyde and acetaldehyde, H-atom abstraction on the α site requires a correction of –4500 cal mol^{-1} to be applied to the activation energy for H-atom abstraction of a primary H-atom from a methyl group. Moreover,

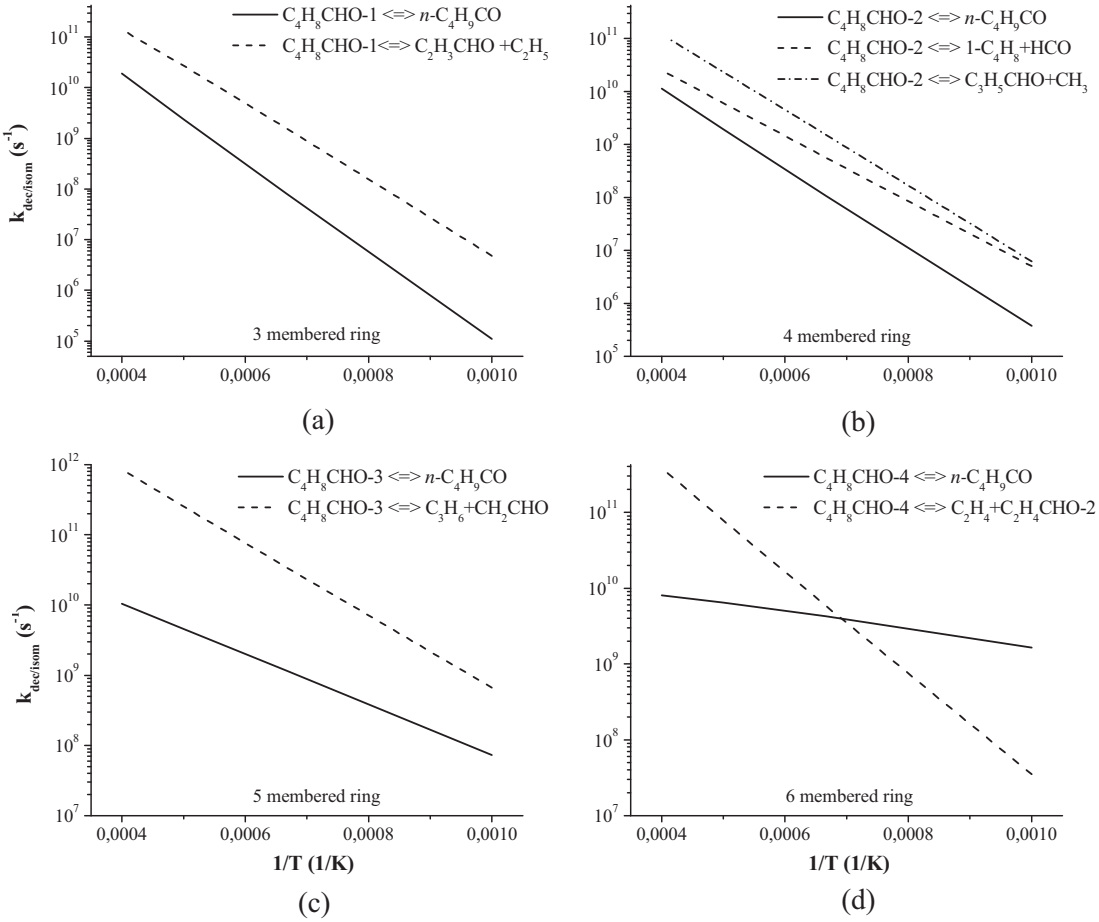

Fig. 9. Isomerization (solid lines) and decomposition (dashed lines) reactions of *n*-pentanal radicals. (a) β-Radical (C_4H_8CHO-1), (b) γ-radical (C_4H_8CHO-2), (c) δ-radical (C_4H_8CHO-3), (d) ε-radical (C_4H_8CHO-4).

Table 7
Experimental data used for the validation of the aldehydes mechanisms.

Aldehyde	Reactor/facility		T (K)	p (atm)	Φ	Ref.
Formaldehyde	Shock tube	Pyrolysis	1160–1890	1.4–2.5	/	Hidaka et al. [34]
	Shock tube	Pyrolysis	1200–2000	1.3–3.0	/	Hidaka et al. [36]
	Shock tube	Pyrolysis	1560–2276	0.9–2.5	/	Eiteneer et al. [33]
	Shock tube	Oxidation	1600–3000	1.0–2.0	0.54, 0.63	Dean et al. [37]
	Shock tube	Oxidation	1160–1618	1.4–2.5	0.25, 0.5, 1.0, 2.0, 4.0	Hidaka et al. [34]
	Shock tube	Oxidation	1334–1974	0.8–2.3	0.16, 0.25, 1.0, 1.7, 5.9	Eiteneer et al. [33]
	Plug flow reactor	Oxidation	945	1.0	1.56	Li et al. [38]
	Plug flow reactor	Oxidation	1095	1.0	0.93	Li et al. [38]
Acetaldehyde	Shock tube	Pyrolysis	1013–1577	1.2–2.8	/	Yasunaga et al. [46]
	Jet stirred reactor	Oxidation	900–1300	1,10	0.09, 0.43, 0.82, 1.0, 1.61	Dagaut et al. [44]
	Shock tube	Oxidation	1276–1703	1.7–2.6	0.2, 0.4, 1	Yasunaga et al. [46]
Propanal	Shock tube	Pyrolysis	970–1300	2.0–2.7	/	Lifshitz et al. [49]
	Shock tube	Pyrolysis	972–1372	1.4–2.8	/	This work
	Shock tube	Oxidation	1170–1750	1.0, 3.0	0.5, 1.0, 2.0	This work
	Shock tube	Oxidation	1150–1560	1.0, 12.0	0.5, 1.0	Akih–Kumgeh [51]
	Premixed flat flame	Oxidation	314–2000	0.05	1.0	Kasper et al. [50]
	Laminar premixed flames	Oxidation	343–2320	1.0	0.75–1.6	Veloo et al. [52]
n-Butanal	Shock tube	Pyrolysis	1096–1368	1.1–2.8	/	This work
	Shock tube	Oxidation	1190–1550	1.7	1.0, 2.0	Davidson et al. [54]
	Shock tube	Oxidation	1180–1580	1.3, 5, 10	0.5, 1.0, 2.0	Zhang et al. [56]
	Shock tube	Oxidation	1224–1634	1.0, 3.0	0.5, 1.0, 2.0	This work
	Laminar premixed flames	Oxidation	343–2320	1.0	0.75–1.6	Veloo et al. [53]
n-Pentanal	Shock tube	Pyrolysis	970–1370	1.4–2.8	/	This work
	Shock tube	Oxidation	1167–1850	1.0, 3.0	0.5, 1.0, 2.0	This work

a greater selectivity of $\dot{H}$ and $H\dot{O}_2$ radicals with respect to the corresponding one of $\dot{O}H$ and $\dot{C}H_3$ radicals is also accounted. With regards to abstraction from the β-site, leading to resonantly stabilized radicals, a correction factor of about 1.25 has been applied to increase the frequency factor of the secondary H-atom abstraction in alkanes. Rate constants for abstraction reactions by $\dot{H}$, $\dot{O}H$, $\dot{C}H_3$ and $H\dot{O}_2$ radicals are listed in the Supplementary Material. Again, the kinetic parameters here proposed for H-abstractions by $\dot{O}H$ radical are further supported by the recent study by Wang et al. [103].

Figure 9 shows that the lifetime of large radicals is so short at high temperatures that they decompose and isomerize without significant interactions with the remaining mixture. When parallel competing reactions are absent or not strongly dependent on temperature, larger radicals can be conveniently and directly substituted by their reaction products. Therefore, it is possible to assume them as being directly transformed into their products which are already part to the C_0—C_4 mechanism [105]. This is the advantage of a lumped approach: it leads to a reduction of the total number of species needed to describe the overall oxidation pro-cess. The analysis of Fig. 9 highlights that only the ε-radical ($\dot{C}_4H_8$-CHO-4) of pentanal shows a temperature dependent competition between isomerization and decomposition rates at high-tempera-tures. Therefore, it is convenient to keep the ε-radical inside the scheme. The four remaining radicals have been assumed to directly transform into their final products. The same assumption has been also applied to the intermediate radicals of *n*-butanal and propanal. The effect of these simplifications has proven to be of very limited importance in the high-temperature range of the analyzed conditions. At low-temperatures, interactions with oxygen forming peroxyl radicals will precede the decomposition of primary radicals; therefore, it would be necessary to increase the detail of the involved species.

The oxidation mechanism adopted here [64] consists of over 10,000 reactions and more than 350 species and was developed based on hierarchical modularity. It covers from hydrogen and oxygenated species, up to diesel and biodiesel fuels. The thermochemical data for most species in the global mechanism were obtained from the CHEMKIN thermodynamic database [106,107]. For those species whose thermodynamic data are not available in the literature, the group additivity method was used to estimate these properties [75].

The overall kinetic model, with thermo and transport properties, is available in CHEMKIN format from: http://creckmodeling.chem.polimi.it and in the Supplementary Material.

5. Model predictions and comparison with experimental data

The new experimental data on pyrolysis speciation and ignition delay times for the three aldehydes were used to validate the aldehyde sub-mechanism in both the kinetic models. Furthermore, propanal pyrolysis data by Lifshitz et al. [49] and ignition delay times by Akih-Kumgeh and Bergthorson [51] were also used. Similarly, *n*-butanal ignition delay times measured by Davidson et al. [54] and by Zhang et al. [56] were also compared with model predictions. Finally, comparisons with premixed laminar flame speeds of propanal and *n*-butanal by Veloo et al. [52,53] complete this kinetic study. The current study, therefore considers all relevant experimental data which exist at present for long chain aldehydes, thus providing a comprehensive evaluation of mechanism performance. A summary of the experimental data at which the aldehydes mechanisms were validated in this study is reported in Table 7.

5.1. Pyrolysis in shock tubes

Propanal pyrolysis of a 1% fuel mixture in argon was studied in a single-pulse shock tube by Lifshitz et al. [49] over the temperature range 1000–1300 K. Experimental data and modeling predictions are shown in Fig. 10 for the NUIG and POLIMI mechanisms. Furthermore, Fig. 11 compares experimental data from this work and predicted concentration profiles for propanal (3%) decomposi-tion in argon. Propanal undergoes decomposition at ~1050 K according to both the experimental data sets and the mechanisms slightly under-predict fuel conversion: an overall good agreement is observed for the main products (CO and C_2H_4), as well as for the minor hydrocarbon species, particularly in terms of their

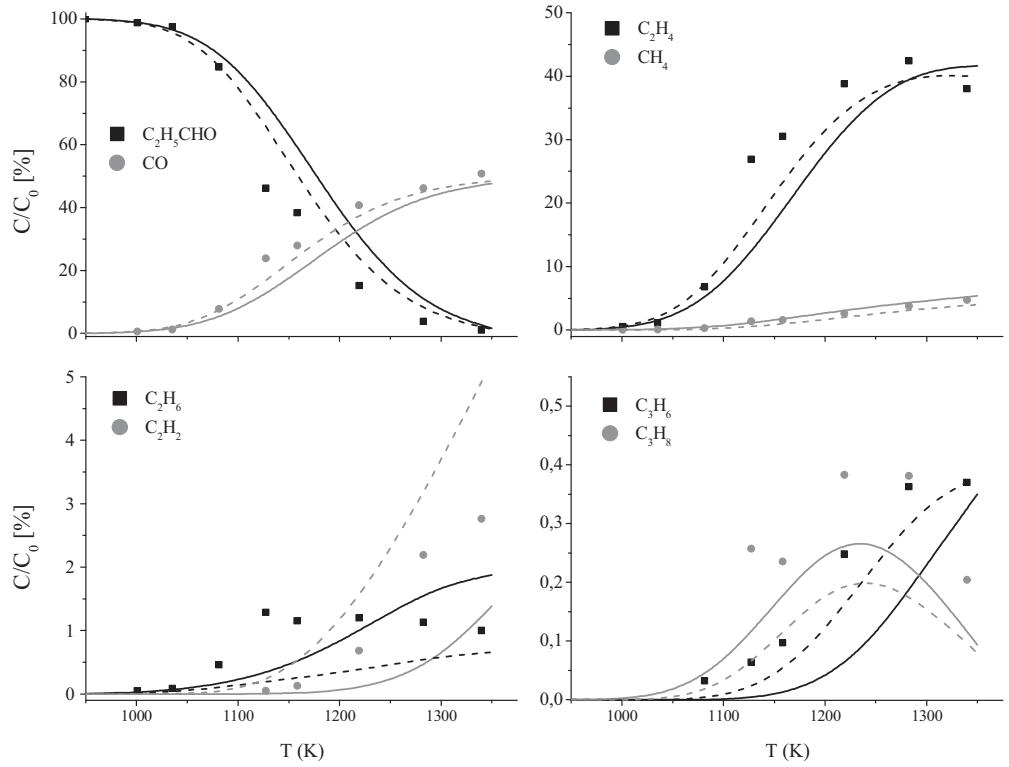

Fig. 10. Predicted and experimental concentration profiles from shock tube pyrolysis of 1% propanal in argon [49] (τ = 2.5 ms). Experimental (symbols), POLIMI mechanism (solid lines) and NUIG mechanism (dashed lines).

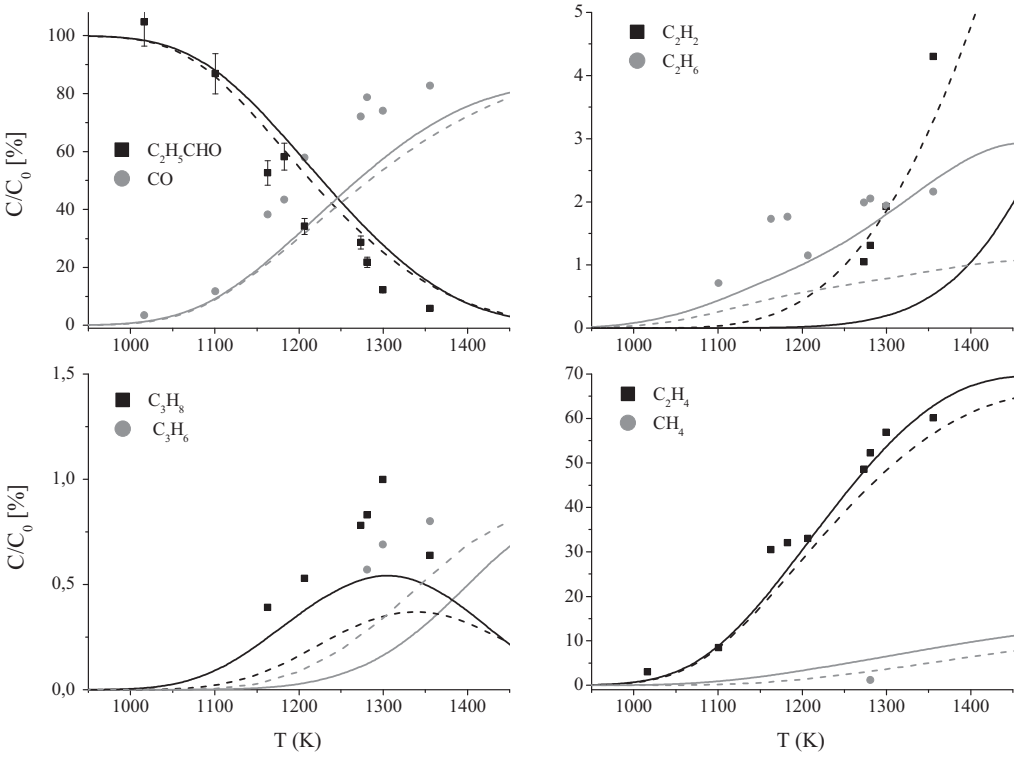

Fig. 11. Predicted and experimental concentration profiles from shock tube pyrolysis of 3% propanal in argon (τ = 2.5 ms). Experiments (symbols), POLIMI mechanism (solid lines) and NUIG mechanism (dashed lines).

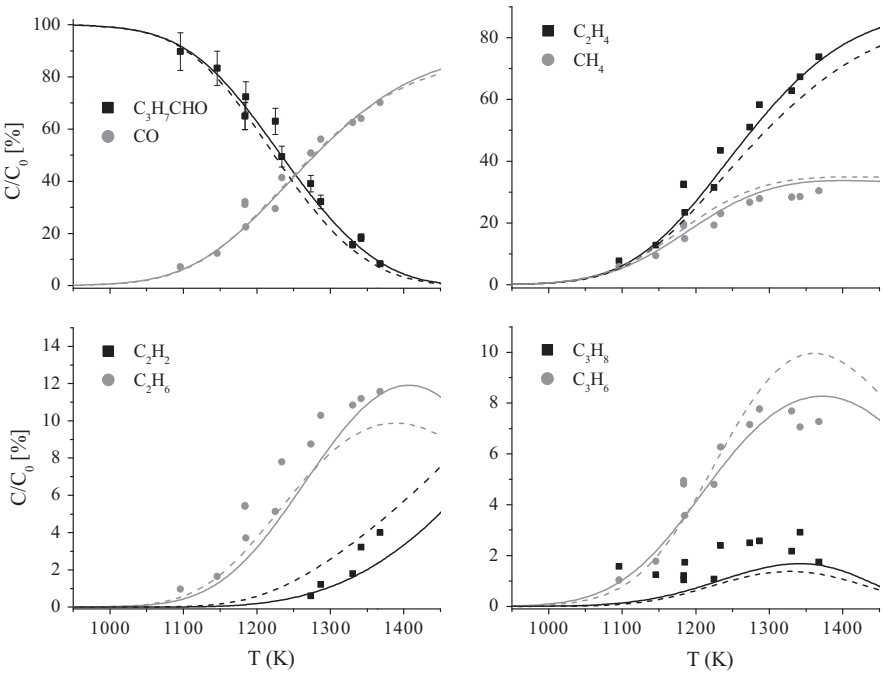

Fig. 12. Predicted and experimental concentration profiles from shock tube pyrolysis of 3% *n*-butanal in argon (τ = 2.0 ms). Experiments (symbols), POLIMI mechanism (solid lines) and NUIG mechanism (dashed lines).

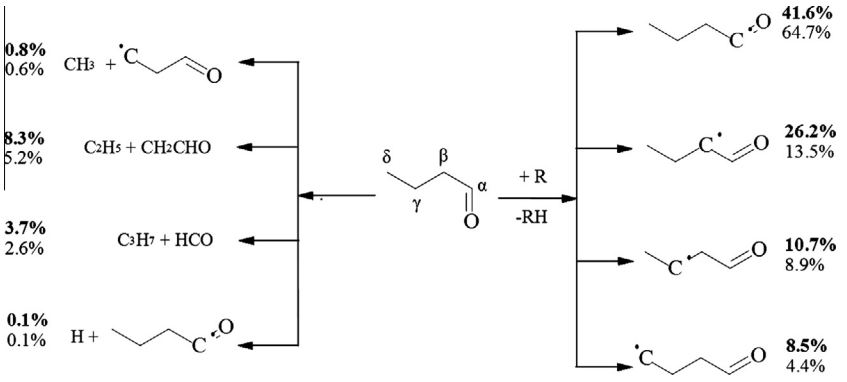

Fig. 13. Global rate of production analysis carried out at 1200 K under the same pyrolysis conditions of Fig. 11, NUIG mechanism (bold) and POLIMI mechanism (standard).

relative concentrations. Analysis of the mechanisms shows that chain radical initiation occurs via unimolecular decomposition reactions involving a C—C bond cleavage, and propanal decomposition mainly occurs via H-atom abstraction reactions by $\dot{H}$ atoms and $\dot{C}H_3$ radicals.

The POLIMI mechanism under-predicts C_2H_2 formation reported in Fig. 10 by ~40% at temperatures higher than 1200 K and even larger deviations are observed in Fig. 11. The chemistry of the vinyl radical ($\dot{C}_2H_3$) is responsible for this under-prediction. H-atom abstractions from acrolein (C_2H_3CHO) are the main pathways generating acetylene, either through the vinyl radical formed by the CO elimination of the α radical, or via the β-scission of the γ radical to give formyl radical. The same chemistry is responsible for the over-prediction of acetylene observed for the NUIG mechanism in Fig. 10, while good agreement is observed in Fig. 11. The under-predictions of propane and propylene can be attributed to a low methyl radical concentration, i.e. a relatively low importance of the chain initiation reactions. The results shown in Figs. 10 and 11 are considered to be well within the expected experimental uncertainties.

Figure 12 compares experimental and predicted concentration profiles for *n*-butanal (3%) decomposition in argon. Predictions of fuel conversion as well as the major products, such as CO and ethylene, are in very good agreement with the experimental observations. Smaller hydrocarbons detected in the measurements (CH_4, C_2H_2, C_2H_6, C_3H_6 and C_3H_8), are also very well captured by both models. The main relative deviations are observed in the trace amount of propane; this under-prediction is due to methyl and ethyl radical recombination. In analogy with the direct formation of methane and CO from acetaldehyde [46], molecular reactions to form CO or ketene and the corresponding C_{n-1} or C_{n-2} alkane are considered, and they play only a limited role under the investigated conditions.

Figure 13 shows a global rate of production analysis performed at 1200 K, for both the NUIG and POLIMI mechanisms. The chain initiation occurs *via* unimolecular decomposition reactions, the successive decomposition of formyl, ethyl and propyl radical intermediates leads to the generation of $\dot{H}$ atoms and $\dot{C}H_3$ radicals, which are responsible, via H-atom abstraction, for ~90% of fuel consumption, at 1200 K.

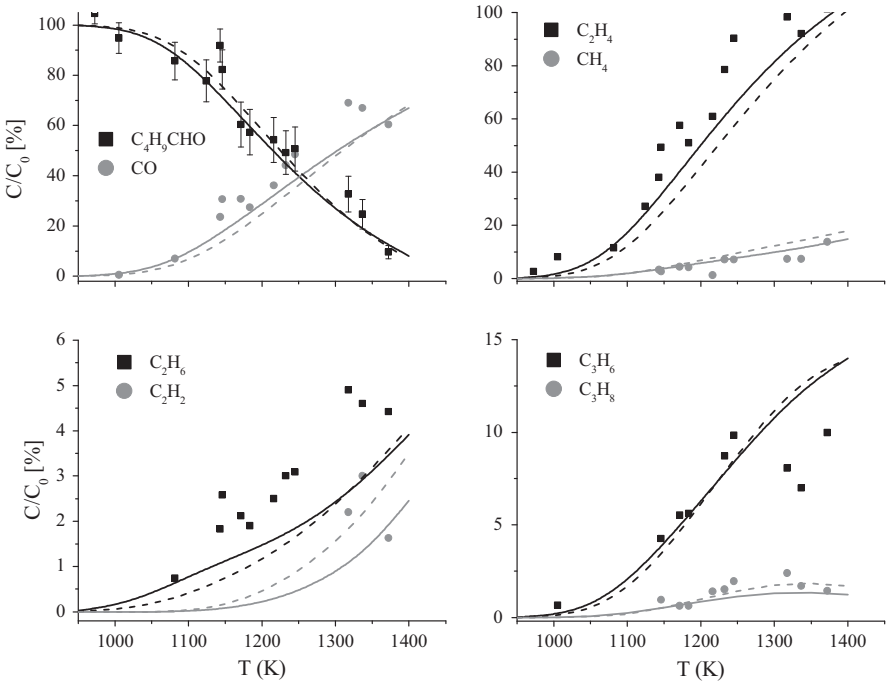

Fig. 14. Predicted and experimental concentration profiles from shock tube pyrolysis of 3% *n*-pentanal in argon (τ = 2.3 ms). Experiments (symbols), POLIMI mechanism (solid lines) and NUIG mechanism (dashed lines).

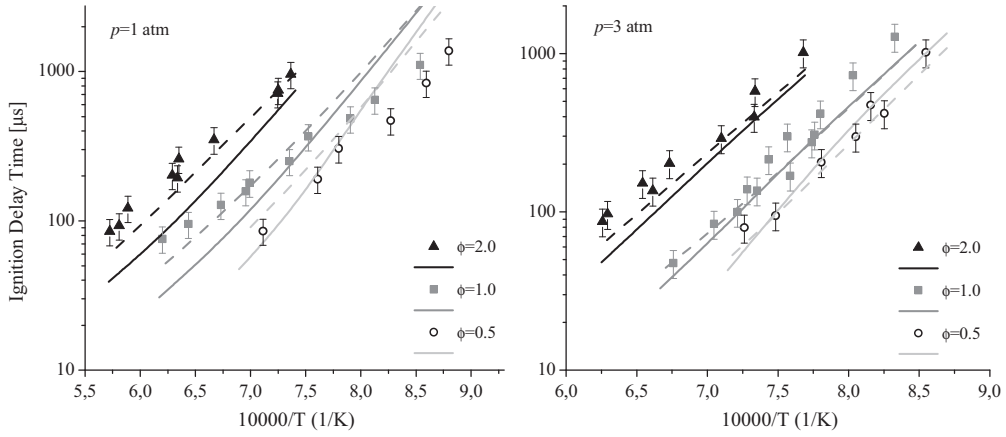

Fig. 15. Predicted and experimental ignition delay times of 1% propanal in O_2/Ar mixtures. Experiments (symbols), POLIMI mechanism (solid lines) and NUIG mechanism (dashed lines).

Figure 14 compares the species predictions by both mechanisms to experimental data for 3% *n*-pentanal pyrolysis in argon. Both of the models are able to reproduce the fuel conversion, indicating that *n*-pentanal starts to decompose at temperatures of ~1000–1050 K. Both of the mechanisms reproduce the relative importance of all species. Within the experimental uncertainty, the two kinetic schemes satisfactorily reproduce the minor hydrocarbon species.

Experimentally, the three aldehydes seem to behave very closely for temperatures up to ~1200 K. Propanal shows the highest conversion rate for T > 1200 K, while no big differences are highlighted between *n*-pentanal and *n*-butanal. As schematically shown in Fig. 5, this can be justified by the fact that the H-abstrac-tion from the highly reactive α and β positions of propanal results in a very high production of H· radical, via β-scission reactions. Both the mechanisms predict very similar reactivity up to ~1200 K, with butanal showing the highest conversion rate for higher temperatures.

Both mechanisms agree with the pyrolytic experiments, indicating that the core pyrolytic kinetics and thermodynamics are of reasonable accuracy. Particularly, both the models satisfactorily reproduce fuel and methane profiles for the three aldehydes, indicating that rate constants for unimolecular decomposition (initiation step), abstraction by hydrogen and methyl radical (propagation steps), and methyl-methyl radical recombination (termination step) are well-constrained.

5.2. Ignition delay times in shock tubes

5.2.1. Propanal

Ignition delay times measurements at 1 and 3 atm reflected pressures made in this study are shown in Fig. 15 together with modeling predictions. Experiments were carried out using 1% fuel in O_2/argon as described in Table 2 (Section 2.2). While the mechanisms are in good or reasonable agreement with the experimental data at 3 atm under all investigated conditions, larger deviation are

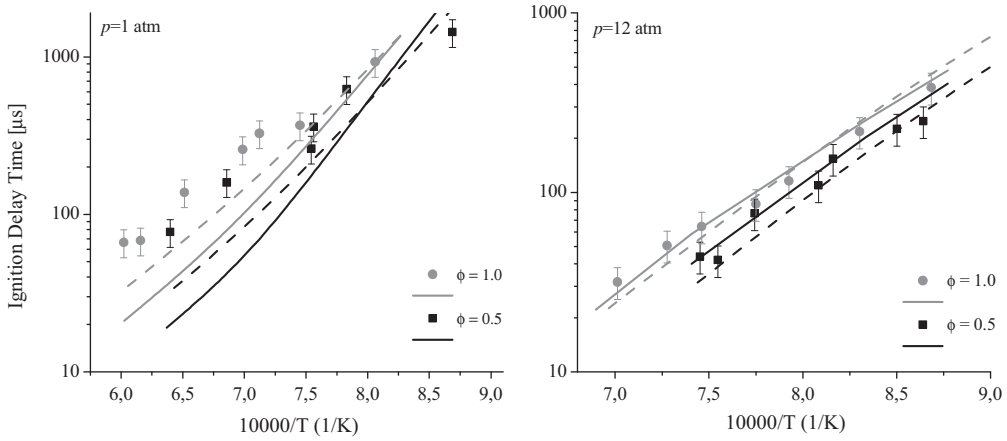

Fig. 16. Predicted and experimental ignition delay times of O_2/Ar mixtures containing 1.25% propanal [51]. Experiments (symbols), POLIMI mechanism (solid lines) and NUIG mechanism (dashed lines).

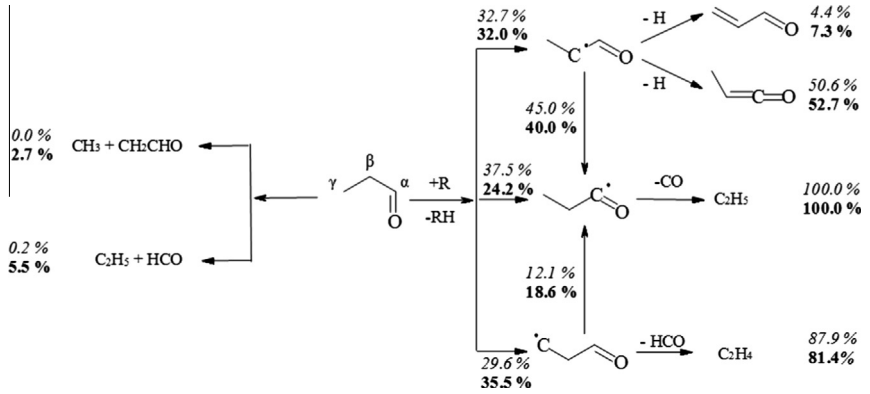

Fig. 17. Rate of production analysis for 1% propanal in O_2/Ar mixtures at φ = 1.0, p = 1 atm. NUIG mechanism, T = 1150 K (italic) and 1620 K (bold).

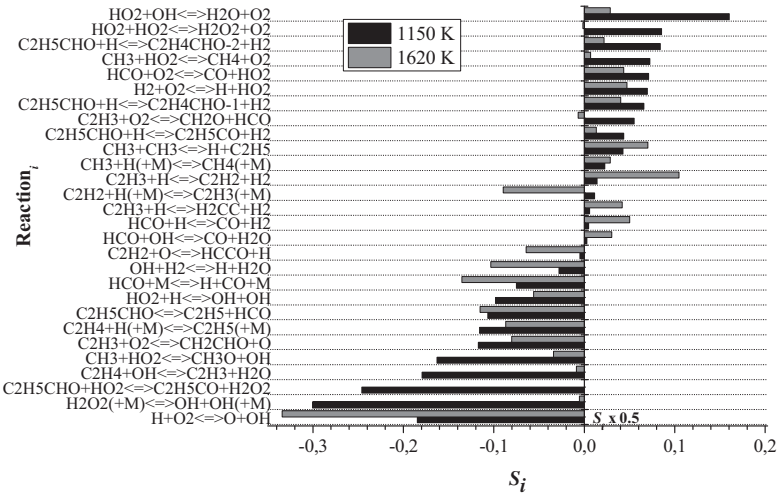

Fig. 18. Sensitivity coefficients of ignition delay times to rate constants for 1% propanal in O_2/Ar mixtures at φ = 1.0, p = 1 atm, 1150 K (black bars) and 1620 K (gray bars). NUIG mechanism.

observed at atmospheric pressure. In this case, both of the mechanisms predict higher apparent activation energies, particularly at stoichiometric and fuel-lean conditions.

Figure 16 compares model predictions and ignition delay times measured by Akih-Kumgeh and Bergthorson [51]. In line with the previous observations of Fig. 15, while good agreement is obtained at 12 atm pressure, at atmospheric pressure the activation energy is over-predicted by both mechanisms. The NUIG mechanism shows better agreement with the data of Akih-Kumgeh, primarily for stoichiometric atmospheric conditions.

Figure 17 shows a global rate of production analysis at stoichiometric conditions, atmospheric pressure, and at temperatures of

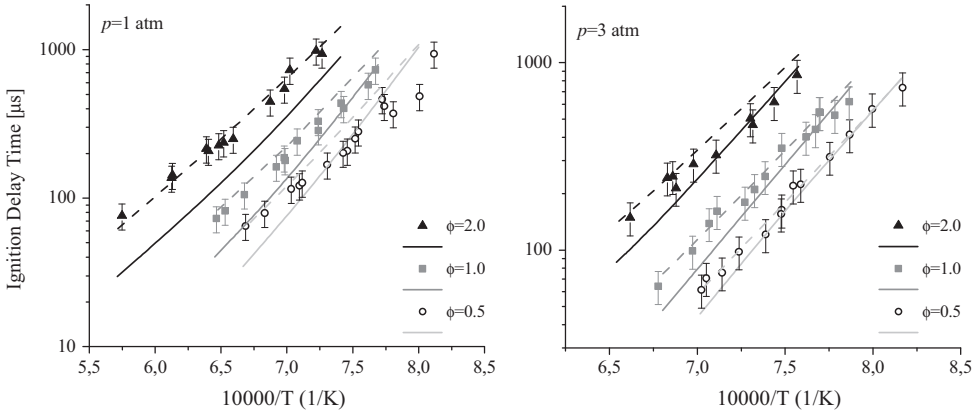

Fig. 19. Predicted and experimental ignition delay times of O_2/Ar mixtures containing 1% *n*-butanal. Experiments (symbols), POLIMI mechanism (solid lines) and NUIG mechanism (dashed lines).

1150 K and 1620 K for the NUIG mechanism. At 1620 K, the unimolecular decomposition pathways contribute ~8% to fuel consumption, being negligible at 1150 K. The fuel decomposition mostly occurs through the α channel, either via direct H-atom abstractions or due to isomerization of β and γ radicals, with a relevant formation of $\dot{C}_2H_5$ radicals. At 1620 K ethyl radicals mostly decompose to ethylene and Ḣ atoms promoting reactivity, while at 1150 K ethyl radicals can also react with molecular oxygen producing $H\dot{O}_2$ radicals, thus inhibiting the system.

Figure 18 shows the sensitivity coefficients of ignition delay times to rate constants in the NUIG mechanism. Sensitivity coefficients were calculated for each reaction via a brute force method, where a negative coefficient indicates a reaction promoting reactivity, i.e. decreases ignition delay times. Increasing the rates of H-atom abstraction reactions by Ḣatoms decreases reactivity mak-ing ignition delay times longer. This is because by reacting with any species but O_2 a Ḣ atom is removed from the system to form H_2, rather than reacting with O_2 to generate Ö atoms and ȮH rad-icals which is the predominant chain-branching process for high temperature combustion. H-atom abstraction by $H\dot{O}_2$ radicals on the α site appears as a sensitive parameter at 1150 K, due to the subsequent decomposition of H_2O_2 to generate two ȮH radicals, which is highlighted as a promoting reaction. The importance of radical species such as formyl, methyl, vinyl and ethyl radicals is also highlighted, confirming the influence of reactions involving β-scission products such as ethylene and acrolein in the correct determination of propanal ignition. It is also of interest to observe the strong competition between vinyl radical decomposition through the third body reaction forming acetylene and Ḣ atom, enhancing reactivity, and the bimolecular disproportionation reaction to form acetylene and H_2, inhibiting reactivity.

5.2.2. n-Butanal

Figure 19 shows a comparison between experimental and calculated ignition delay times for mixture of 1% *n*-butanal in O_2/argon. Both of the mechanisms agree with the experimental data at the conditions tested, with the NUIG mechanism being consistently slower compared to the POLIMI mechanism, particularly at atmospheric and fuel rich conditions. The larger deviations from the experimental observations, mainly in terms of apparent activation energies, can be observed for the POLIMI and NUIG mechanisms at 1 atm and $\varphi = 0.5$.

Figure 20 compares the mechanisms predictions with the experimental measurements of Davidson et al. [54], at two different dilutions. The NUIG mechanism reproduces the apparent activation energy in both cases, while the POLIMI mechanism, slightly

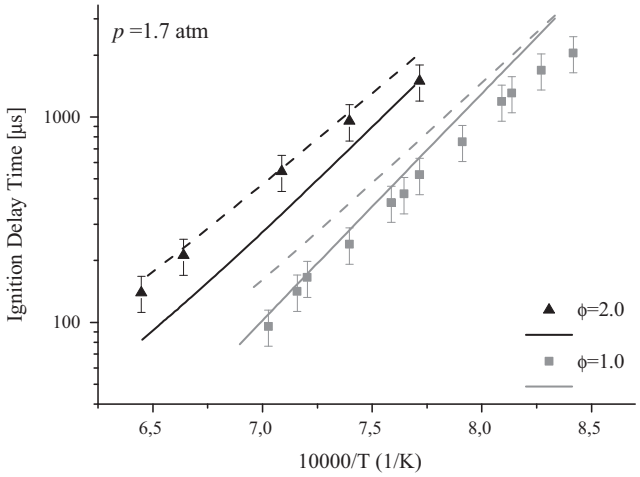

Fig. 20. Predicted and experimental ignition delay times of O_2/Ar mixtures containing 1% *n*-butanal [54]. Experiments (symbols), POLIMI mechanism (solid lines) and NUIG mechanism (dashed lines).

faster than NUIG, over-predicts the activation energies, but is still in reasonable agreement with experiments.

Figure 21 compares all three sets of experimental data (our experiments at 1 atm, Zhang et al. [56] at 1.3 atm and Davidson et al. [54] at 1.7 atm). Following the approach of Davidson et al. [54], all of the data have been scaled at 1.7 atm, assuming a scaling factor $p_{exp}/1.7^{-0.52}$. The experimental data agree under stoichiometric conditions, while the measurements of Zhang are notably faster under fuel-rich conditions. Figure 22 compares the experimental data from Zhang et al. [56] with model predictions. Both of the mechanisms tend to over-predict ignition delay times, particularly at 1.3 atm. The POLIMI mechanism reproduces these experiments more closely than the NUIG mechanism, which over-predicts the ignition delay times, particularly at atmospheric pressure. However, on the basis of the observations of Fig. 21, the performances of the two mechanisms are considered to be in satisfactory agreement with the experimental data.

Figure 23 shows a reaction path analysis carried out for fuel-lean ($\varphi = 0.5$) and fuel-rich ($\varphi = 2.0$) mixtures at 3 atm and 1320 K, with the NUIG mechanism. The unimolecular decomposition reactions accounts for 12.6% and 7.5% of fuel consumption under fuel-rich and fuel-lean conditions, respectively. H-atom abstraction from the α site is an important decomposition channel (~27.0%). The β and γ sites show similar selectivities (20–30%), with β favored at fuel-rich conditions and γ at fuel-lean conditions.

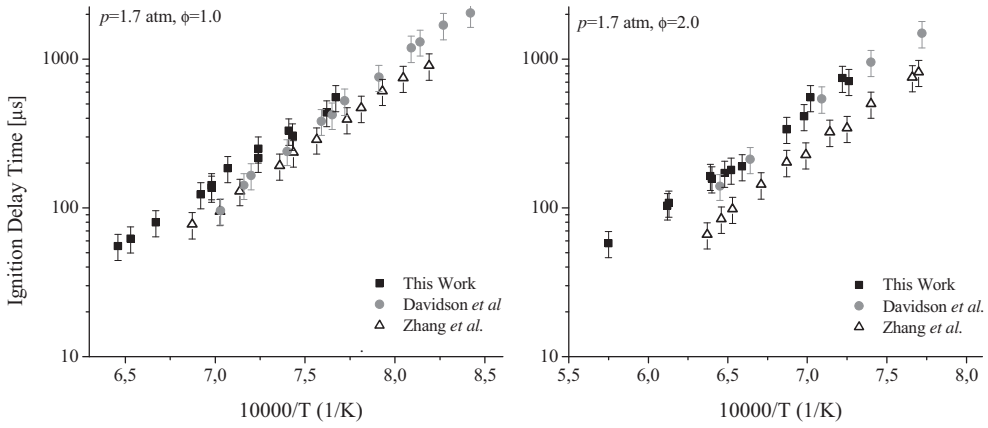

Fig. 21. Comparison amongst experimental ignition delay times for *n*-butanal-O_2/Ar mixtures, scaled at 1.7 atm. This work: 1% fuel at 1 atm (squares); Zhang et al. [56]: 1.2%fuel at 1.3 atm (triangles); Davidson **et al.** (circles) [54]: 1% fuel at 1.7 atm.

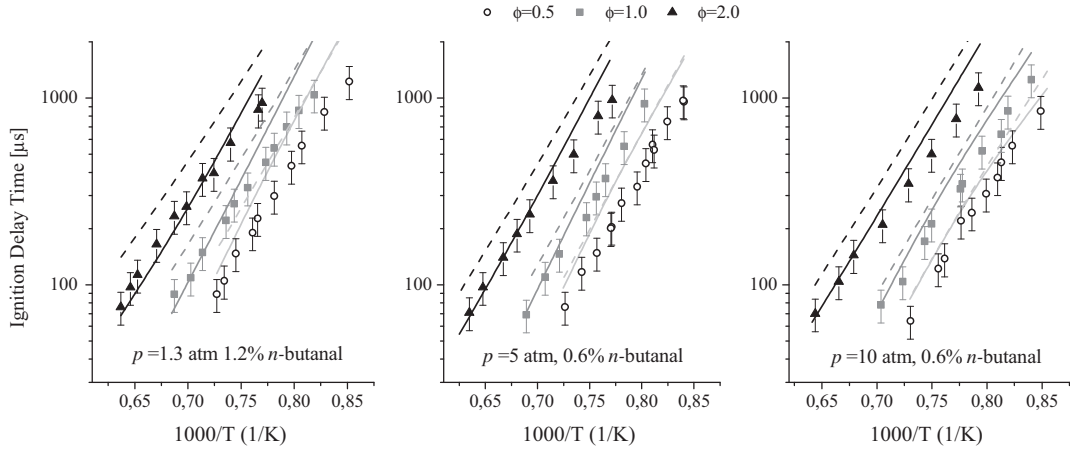

Fig. 22. Predicted and experimental ignition delay times of *n*-butanal in O_2/Ar mixtures [56]. Experiments (symbols), POLIMI mechanism (solid lines) and NUIG mechanism (dashed lines).

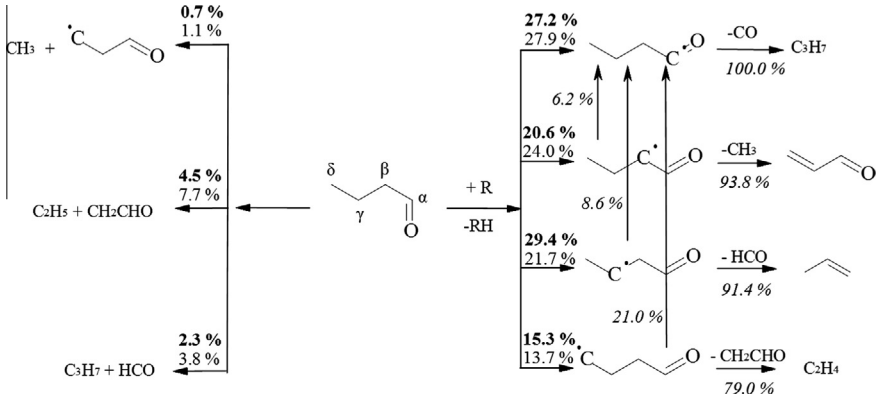

Fig. 23. Rate of production analysis for 1% *n*-butanal in O_2/Ar mixtures at p = 3 atm, T = 1320 K at φ = 0.5 (bold) and φ = 2.0 (standard).

This can be explained on the basis of a higher production of $\dot{O}H$ radicals through the chain-branching reaction $\dot{H} + O_2 \leftrightarrow \ddot{O} + \dot{O}H$, due to the higher concentration of oxygen in the system. $\dot{O}H$ radicals are then more likely to abstract on the γ site relative to the β site.

Figure 24 presents sensitivity coefficients of ignition delay times to rate constants for NUIG mechanism at the same condi-tions shown in Fig. 23, in order to identify the reactions controlling the auto-ignition behavior. Chain initiation reactions generating highly reactive radicals promote the system's reactivity at both conditions. Particularly, the breaking of the weak C_β—C_γ bond producing an ethyl radical and the breaking of the C_α—C_β bond producing a formyl radical exhibit some sensitivity. Decreasing the oxygen concentration largely enhances the importance of small unsaturated species such as acetylene, ethylene, propylene and the parent radicals. H-atom abstraction reaction by $\dot{H}$ atoms reduces the reactivity due to the competition with the branching reaction $\dot{H} + O_2 \leftrightarrow \ddot{O} + \dot{O}H$. Furthermore, H-atom abstractions from

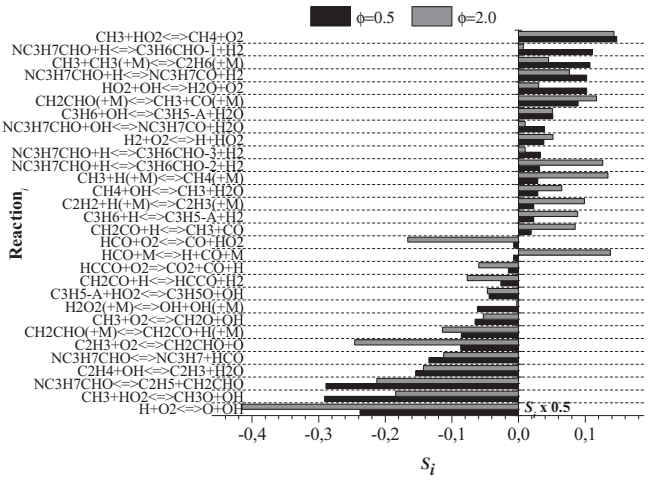

Fig. 24. Sensitivity coefficients of ignition delay times to rate constants for 1% *n*-butanal in O_2/Ar mixtures at p = 3 atm, T = 1320 K at φ = 0.5 (black bars) and φ = 2.0 (gray bars).

the α site increase the ignition delay times due to the formation of 1-propyl radical, which mainly decomposes to produce methyl radicals. Analyses carried out for POLIMI mechanisms highlighted the same classes of fuel specific reactions as sensitive to the ignition delay time determination.

5.2.3. n-Pentanal

Experimental and calculated ignition delay times for 1% *n*-pentanal mixtures in O_2/Ar are reported in Fig. 25 for conditions as described in Table 2. The NUIG mechanism captures the experimental data at every condition tested. The POLIMI mechanism tends to predict shorter ignition delay times for fuel-rich conditions particularly at atmospheric pressure. At 1850 K, the ignition delay time is under-predicted by a factor of three. Again, the model over-predicts the apparent activation energy. At 3 atm both of the models over-estimate the ignition delay time at fuel-lean conditions for temperatures below 1100 K. Low-temperature chemistry, outside the scope of this work, might have an effect at these conditions.

Figure 26 presents a rate of production analysis carried out for the POLIMI mechanism at intermediate conditions (φ = 1.0, p = 2 atm, T = 1300 K). Unimolecular decomposition reactions account for less than 3.0% of *n*-pentanal consumption. Decomposition occurs mainly via H-atom abstraction from the α position (∼54%), followed by abstraction from the γ and δ (∼15%) positions. At the conditions investigated ∼75% of the ε-radical ($\dot{C}_4H_8CHO$-4) isomerizes to the α-radical (n-$C_4H_9\dot{C}O$), which is assumed to eliminate CO (90%) and/or decompose to *n*-propyl and ketene (10%). As already discussed in Section 4.2, the POLIMI lumped mechanism only accounts for the ε-radical, the rate of production is simply obtained through a *de-lumping* procedure.

Figure 27 shows the sensitivity analyses of ignition delay times to rate constants for the NUIG and POLIMI mechanisms, at φ = 1.0, p = 2 atm, and T = 1300 K. With regards to fuel specific reactions,

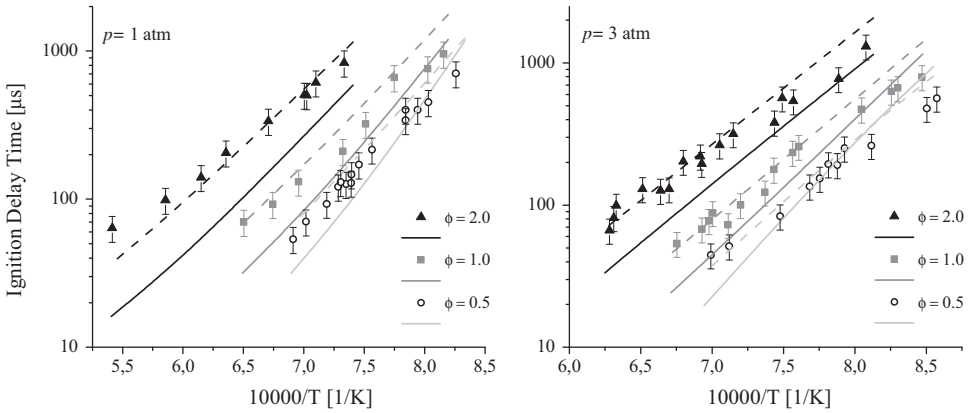

Fig. 25. Predicted and experimental ignition delay times of O_2/Ar mixtures containing 1% *n*-pentanal. Experiments (symbols), POLIMI mechanism (solid lines) and NUIG mechanism (dashed lines).

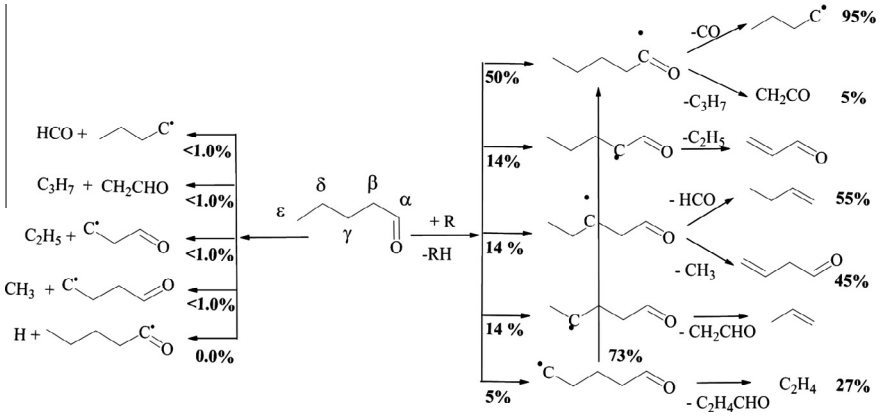

Fig. 26. Rate of production analysis for 1% *n*-pentanal in O_2/Ar mixtures at φ = 1.0, p = 2 atm, T = 1300 K, POLIMI mechanism.

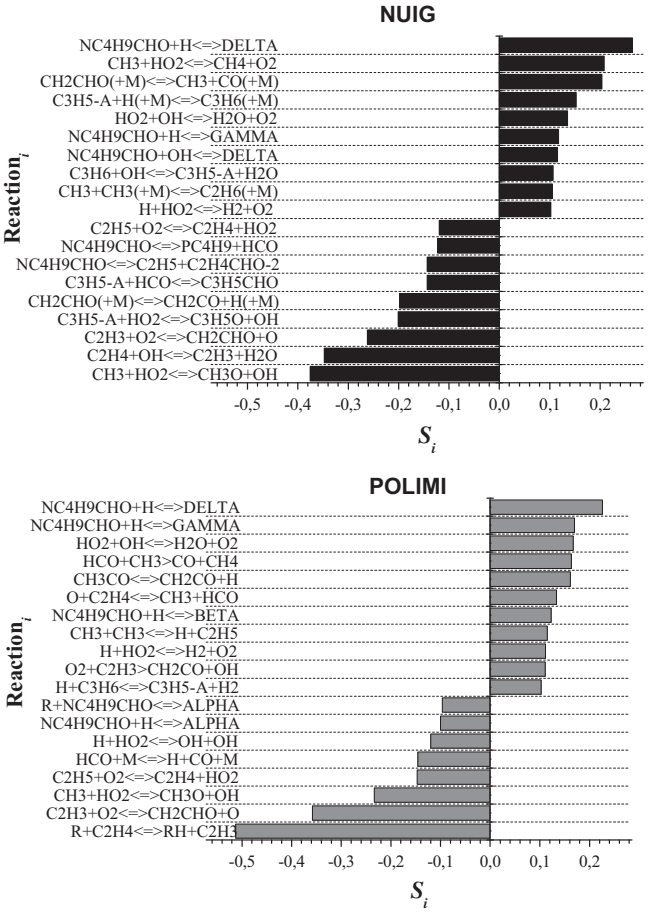

Fig. 27. Sensitivity coefficients of ignition delay times to rate constants for 1% n-pentanal in O_2/Ar mixtures at φ = 1.0, p = 2 atm, T = 1300 K. NUIG mechanism (black bars), POLIMI mechanism (gray bars).

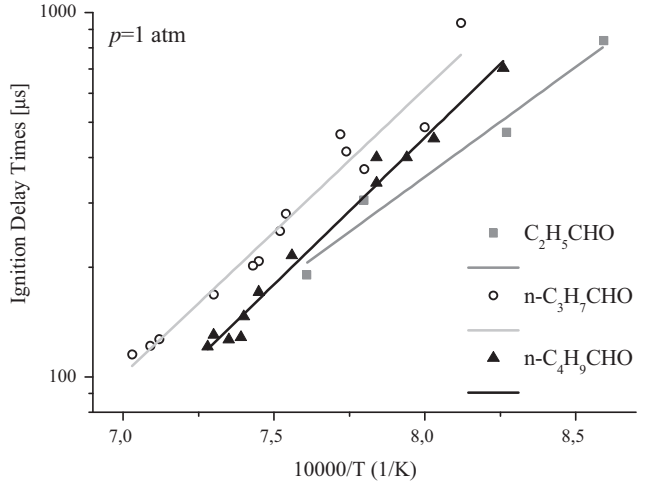

Fig. 28. 1% Fuel–O_2/Ar mixtures; φ = 0.5, p = 1 atm, experimental data from present work (symbols) and linear fit (lines).

both of the mechanisms show that H-atom abstraction rates from the γ and δ positions have positive coefficients, i.e. they decrease reactivity (longer ignition delay times). Unimolecular initiation reactions enhance reactivity in the NUIG mechanism, whilst they are not highlighted as sensitive for the POLIMI mechanism. H-atom

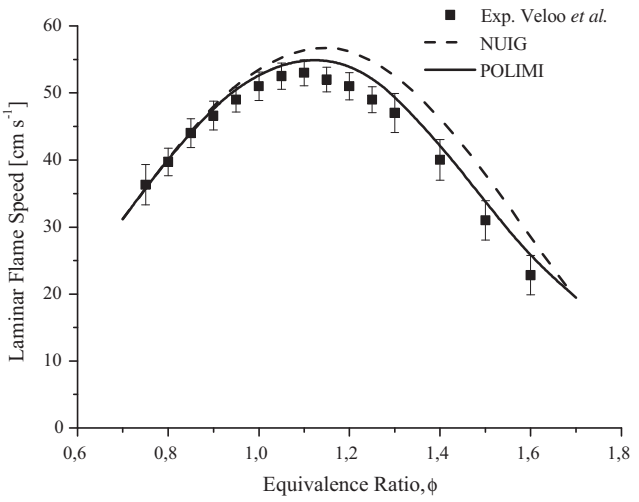

Fig. 29. Experimental and computed laminar flame speeds of propanal/air flames at T_u = 343 K and p = 1 atm. Experimental data (symbols) by Veloo et al. [52], POLIMI mechanism (solid lines) and NUIG mechanism (dashed lines).

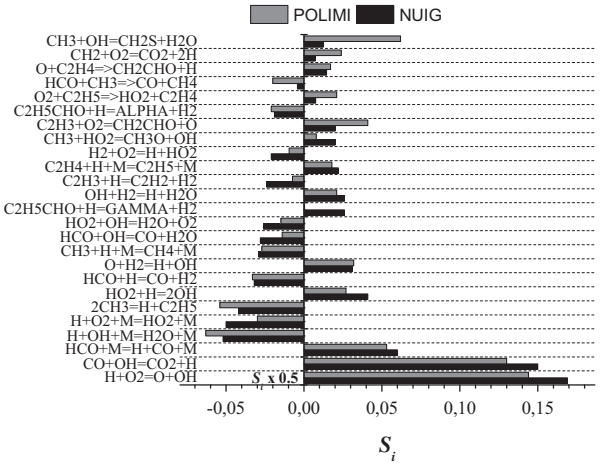

Fig. 30. Sensitivity coefficients of laminar flame speed to rate constants for propanal/air flames at φ = 1.3, T_u = 343 K [52]. NUIG mechanism (black bars) and POLIMI mechanism (gray bars).

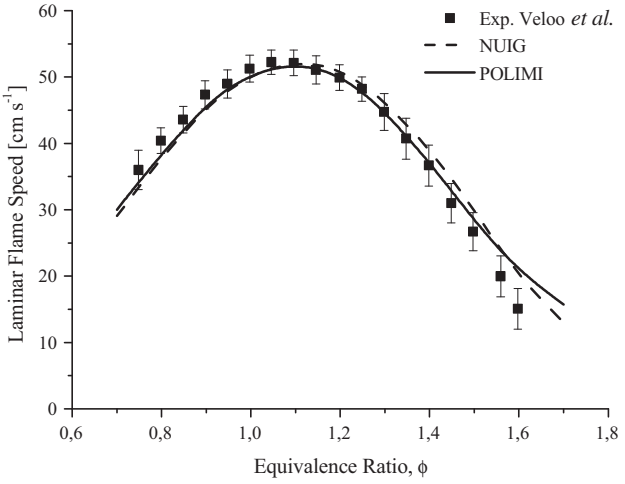

Fig. 31. Experimental and computed laminar flame speeds of *n*-butanal/air flames at T_u = 343 K and p = 1 atm [53]. Experimental data (symbols) by Veloo et al. [53], POLIMI mechanism (solid lines) and NUIG mechanism (dashed lines).

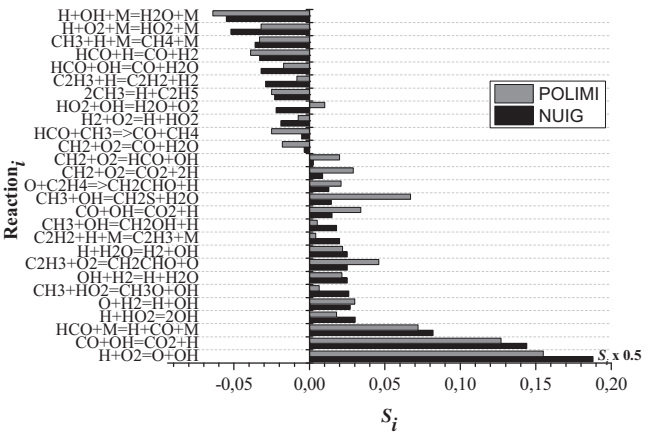

Fig. 32. Sensitivity coefficients of laminar flame speed to rate constants for *n*-butanal/air flames at $\varphi = 1.0$ $T_u = 343$ K [53]. NUIG mechanism (black bars) and POLIMI mechanism (gray bars).

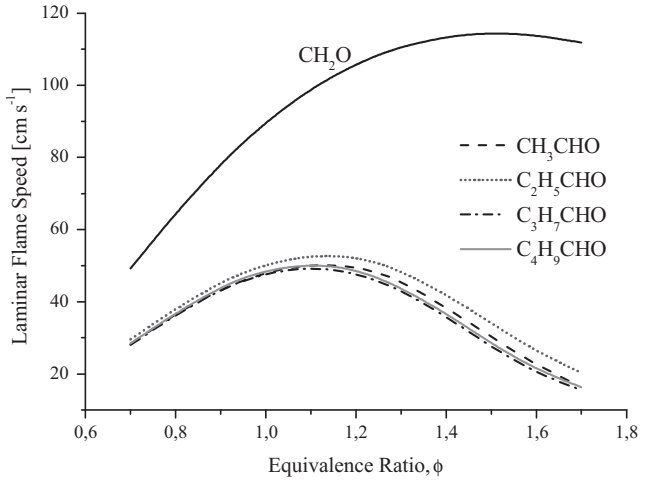

Fig. 33. Comparisons of computed laminar flame speeds (POLIMI mechanism) of aldehyde/air at $T_u = 343$ K and $p = 1$ atm.

abstractions from the α position contribute to shortened ignition delay times for the POLIMI mechanism. Once again, the higher importance of the C_0—C_4 sub-mechanism is highlighted. To make the comparison more clear, the most sensitive branching reaction $\dot{H} + O_2 \leftrightarrow \ddot{O} + \dot{O}H$, normalized to −1 for both the mechanisms, is not reported in Fig. 27.

5.3. Apparent activation energy of ignition delay times

Figure 28 compares the experimental ignition delay times at 1 atm and lean conditions for the three aldehydes. Propanal tends to be the faster to ignite, followed by *n*-pentanal and *n*-butanal. At 1% fuel concentration, due to the larger amount of oxygen, one would expect *n*-pentanal to be the fastest to ignite followed by *n*-butanal and propanal. On the contrary propanal is the most reac-tive and this trend is correctly reproduced by both of the mecha-nisms. In fact, a greater amount of Ḣ atoms is produced by primary propagation reactions during propanal oxidation, while methyl radicals are formed via the decomposition of β and γ radi-cals in *n*-butanal and *n*-pentanal, respectively. This figure also highlights a lower apparent activation energies for propanal (∼25 kcal mol^{-1}) with respect to C_4 and C_5 aldehydes (∼35–40 kcal mol^{-1}). The experimental data of Akih-Kumgeh and Berg-thorson [51], Zhang et al. [56], and Davidson et al. [54] confirm these average values. As far as the predicted activation energies are concerned, the averages of previous simulations show that the NUIG mechanism over-estimates the activation energy of ∼5 kcal mol^{-1}, while the POLIMI mechanism exceeds by ∼10 kcal mol^{-1}. The largest deviations are observed in both cases for fuel-lean conditions. While these deviations need to be better investigated, it is important to observe that they are largely due to the C_0—C_4 mechanism.

5.4. Laminar flame speeds

5.4.1. Propanal

Figure 29 shows a comparison of experimental [52] and predicted laminar flame speeds for propanal/air mixtures at atmospheric pressure. Experimental (53 cm s^{-1}) and predicted peaks (52.7 cm s^{-1} and 56.7 cm s^{-1} respectively for POLIMI and NUIG mechanism) are correctly placed at $\varphi = 1.1$–1.15. NUIG mechanism over-predict the laminar flame speed at stoichiometric and fuel-rich conditions by 2–4 cm s^{-1}. POLIMI mechanism well reproduces the flame speed all over the equivalence ratio range explored. Accounting for the experimental uncertainty represented in Fig. 29 by the error bars (3.5–12.5%), the overall agreement of the mechanisms seems quite satisfactory.

Figure 30 reports the sensitivity coefficients of laminar flame speed to rate constants for propanal/air flames at $\varphi = 1.3$, $T_u = 343$ K, using both mechanisms. H-atom abstraction reaction

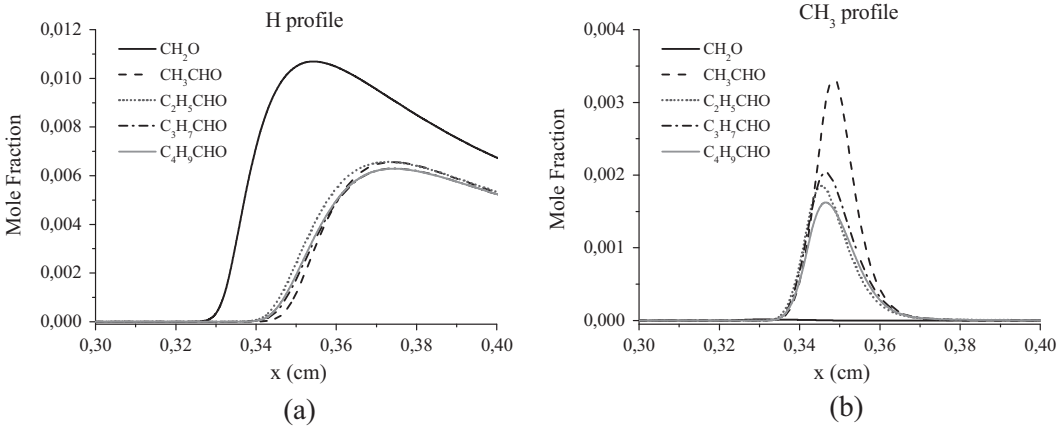

Fig. 34. Computed (POLIMI mechanism) Ḣ (a) and ĊH$_3$ (b) profiles for aldehyde/air flames at $\varphi = 1.0$, $T_u = 343$ K and $p = 1$ = atm.

from the α site are sensitive in reducing the flame speed for both mechanisms. H-atom abstraction from the γ site has a positive sensitivity coefficient (flame propagation enhancer) in the NUIG mechanism. This is due to the fact that, while the γ radical forms $\dot{H}$ and CO from $H\dot{C}O$, ethyl radical can also react with a $\dot{H}$ atom forming two methyl radicals. Results confirm that the chemistry of propanal at flame temperatures is dominated by the C_0—C_2 portion of the mechanisms.

5.4.2. n-Butanal

Experimental [53] and calculated laminar flame speeds for *n*-butanal/air mixtures at atmospheric pressure are reported in Fig. 31. Both the mechanisms are able to well reproduce the experimental measurements for any dilution condition. Sensitivity analyses of flame speeds to rate constants have been carried out for both mechanisms at stoichiometric conditions, the results of which are reported in Fig. 32. Again, the chemistry is mainly controlled by the C_0—C_4 sub-mechanism. Apart from the highly sensitive reactions involving $\dot{H}$, $\dot{C}H_3$, $H\dot{C}O$ and $\dot{O}H$ radicals, also vinyl radical and ethylene chemistry controls the flame speed predictions.

NUIG mechanism is slightly faster than POLIMI in flame speeds predictions, with peak values being 2–4 cm s^{-1} higher. This is in contrast with the previous comments on ignition delay times. This fact supports the key role played by the C_0—C_4 sub-mechanisms, but also shows that key reactions for ignition delay times are different from those more sensitive for laminar flame speeds.

5.5. Comparisons of aldehydes/air laminar flame speeds

Figure 33 compares predicted laminar flame speeds of C_1—C_5 aldehydes/air mixtures at T_u = 343 K and atmospheric pressure. Formaldehyde flame speed peaks at ∼115 cm s^{-1} and equivalence ratio φ of ∼1.5. This behavior can be justified on the basis of both the higher production of $\dot{H}$ and the absence of $\dot{C}H_3$ radicals, with respect to the other aldehydes, as clearly highlighted by Fig. 34. The oxidation of formaldehyde at high temperatures completely occurs through the formation of $H\dot{C}O$, which is rapidly decomposed to $\dot{H}$ + CO through a third body reaction. To the best of our knowl-edge, experimental measurements of formaldehyde flame speeds are not available in literature. Remaining aldehydes show peaks of 50 ± 2 cm s^{-1}, at equivalence ratios of ∼1.1–1.15. The higher concentration of methyl radical shown by acetaldehyde (Fig. 34b) justifies its lower flame speed, with respect to propanal's. Experimentally [52,53], propanal flames propagate slightly faster relative to *n*-butanal flames, particularly at rich conditions. This trend is well captured by both NUIG and POLIMI mechanisms. Once again, Fig. 34a supports this observation showing a slightly higher $\dot{H}$ concentration in the propanal flame with respect to those of *n*-butanal and *n*-pentanal.

6. Conclusions

An experimental and kinetic modeling study of the high temperature pyrolysis and oxidation of C_3—C_5 *n*-aldehydes is presented in this work.

New experimental data have been provided for both pyrolysis and oxidation in shock tubes. Species profile measurements were carried out for the three aldehydes in a single pulse shock tube under pyrolytic conditions. Ignition delay times were measured for 1% fuel O_2/Ar mixtures at 1 and 3 atm in a UV emission shock tube for propanal, *n*-butanal and *n*-pentanal. In both oxidative and pyrolytic environment, propanal showed reactivity higher or at least comparable with that of *n*-pentanal, with *n*-butanal being the less reactive aldehyde.

For the first time the homologous series of C_3—C_5 has been analyzed in detail. Based on previously developed C_1 and C_2 aldehydes mechanisms, a detailed mechanism for the pyrolysis and oxidation of aldehydes was developed and discussed. The mechanism has been coupled with the C_0—C_4 kinetic mechanism of NUIG and of POLIMI, requiring adjustments of H-abstraction reactions within the uncertainties of theoretical calculations, which depend on each specific kinetic environment and approach. Both of the resulting mechanisms were then validated and compared with the complete set of experimental data. Both mechanisms were able to closely reproduce the pyrolysis data, including major and minor species, within the experimental uncertainty. Ignition delay times were also satisfactorily captured by both mechanisms, with the NUIG mechanism being systematically less reactive than the POLIMI one, particularly at low pressures.

Laminar flame speeds of propanal and *n*-butanal were also quite satisfactorily compared with experimental measurements. A comparison of calculated C_1—C_5 aldehydes/air flames allowed insights on important reactions and radical species governing aldehydes flame propagation. Laminar flame speed measurements for formaldehyde and acetaldehyde, missing from the literature at present, could be useful to completely characterize the high temperature oxidation behavior of aldehydes.

Despite the different H-abstraction reaction rates in the two mechanisms, the kinetic analysis highlighted the same fuel specific reactions as being sensitive in the investigated conditions and, furthermore, the relevant role of the two different C_0—C_4 sub-mechanisms. The major differences between the models and the experiments have to be attributed to the chemistry of the smaller species, more than to aldehyde specific reactions (including H-abstractions). This observation further supports the need of an highly accurate C_0—C_4 sub-mechanism, well validated over the wider range of conditions possible as discussed in previous works by Metcalfe et al. [62], Naik et al. [108] and by Ranzi et al. [64].

Appendix A. Supplementary material

Supplementary data associated with this article can be found, in the online version, at http://dx.doi.org/10.1016/j.combustflame.2014.07.027.

References

[1] D. Grosjean, Environ. Sci. Technol. 16 (5) (1982) 254–262.
[2] A. Frassoldati, A. Cuoci, T. Faravelli, U. Niemann, E. Ranzi, R. Seiser, K. Seshadri, Combust. Flame 157 (1) (2010) 2–16. http://dx.doi.org/10.1016/j.combustflame.2009.09.002.
[3] C. Togbé, P. Dagaut, F. Halter, F. Foucher, Energy Fuels 25 (2) (2011) 676–683, http://dx.doi.org/10.1021/ef101485q.
[4] B. Galmiche, C. Togbé, P. Dagaut, F. Halter, F. Foucher, Energy Fuels 25 (5) (2011) 2013–2021, http://dx.doi.org/10.1021/ef2003552.
[5] X. Man, C. Tang, J. Zhang, Y. Zhang, L. Pan, Z. Huang, C.K. Law, Combust. Flame 161 (3) (2014) 644–656.
[6] G. Black, H.J. Curran, S. Pichon, J.M. Simmie, V. Zhukov, Combust. Flame 157 (2) (2010) 363–373. http://dx.doi.org/10.1016/j.combustflame.2009.07.007.
[7] S.M. Sarathy, M.J. Thomson, C. Togbé, P. Dagaut, F. Halter, C. Mounaim-Rousselle, Combust. Flame 156 (4) (2009) 852–864. http://dx.doi.org/10.1016/j.combustflame.2008.11.019.
[8] S.M. Sarathy, S. Vranckx, K. Yasunaga, M. Mehl, P. Oßwald, W.K. Metcalfe, C.K. Westbrook, W.J. Pitz, K. Kohse-Höinghaus, R.X. Fernandes, H.J. Curran, Combust. Flame 159 (6) (2012) 2028–2055. http://dx.doi.org/10.1016/j.combustflame.2011.12.017.
[9] R. Grana, A. Frassoldati, T. Faravelli, U. Niemann, E. Ranzi, R. Seiser, R. Cattolica, K. Seshadri, Combust. Flame 157 (11) (2010) 2137–2154. http://dx.doi.org/10.1016/j.combustflame.2010.05.009.
[10] A. Frassoldati, R. Grana, T. Faravelli, E. Ranzi, P. Oßwald, K. Kohse-Höinghaus, Combust. Flame 159 (7) (2012) 2295–2311. http://dx.doi.org/10.1016/j.combustflame.2012.03.002.
[11] S.S. Vasu, S.M. Sarathy, Energy Fuels 27 (11) (2013) 7072–7080, http://dx.doi.org/10.1021/ef401406z.
[12] C. Togbé, F. Halter, F. Foucher, C. Mounaim-Rousselle, P. Dagaut, Proc. Combust. Inst. 33 (1) (2011) 367–374. http://dx.doi.org/10.1016/j.proci.2010.05.003.

[13] S. Mani Sarathy, S. Park, B.W. Weber, W. Wang, P.S. Veloo, A.C. Davis, C. Togbe, C.K. Westbrook, O. Park, G. Dayma, Z. Luo, M.A. Oehlschlaeger, F.N. Egolfopoulos, T. Lu, W.J. Pitz, C.-J. Sung, P. Dagaut, Combust. Flame 160 (12) (2013) 2712–2728. http://dx.doi.org/10.1016/j.combustflame.2013.06.022.

[14] K.A. Heufer, S.M. Sarathy, H.J. Curran, A.C. Davis, C.K. Westbrook, W.J. Pitz, Energy Fuels 26 (11) (2012) 6678–6685, http://dx.doi.org/10.1021/ef3012596.

[15] K. Yasunaga, T. Mikajiri, S.M. Sarathy, T. Koike, F. Gillespie, T. Nagy, J.M. Simmie, H.J. Curran, Combust. Flame 159 (6) (2012) 2009–2027. http://dx.doi.org/10.1016/j.combustflame.2012.02.008.

[16] P.-J. He, J.-F. Tang, N. Yang, J.-J. Fang, X. He, L.-M. Shao, J. Air Waste Manage. Assoc. 62 (4) (2012) 461–470. http://dx.doi.org/10.1080/10962247.2012.658954.

[17] D. Grosjean, E. Grosjean, A.W. Gertler, Environ. Sci. Technol. 35 (1) (2000) 45–53, http://dx.doi.org/10.1021/es001326a.

[18] E. Zervas, Fuel 87 (7) (2008) 1141–1147. http://dx.doi.org/10.1016/j.fuel.2007.06.010.

[19] G. Karavalakis, S. Poulopoulos, E. Zervas, Fuel 102 (0) (2012) 85–91. http://dx.doi.org/10.1016/j.fuel.2012.05.030.

[20] R. d. Abrantes, J.V. d. Assunção, E.Y. Hirai, Rev. Saúde Públ. 39 (2005) 479–485.

[21] M.M. Roy, Energy Convers. Manage. 49 (5) (2008) 1111–1118, http://dx.doi.org/10.1016/j.enconman.2007.09.014.

[22] J.J. Schauer, M.J. Kleeman, G.R. Cass, B.R.T. Simoneit, Environ. Sci. Technol. 36 (6) (2002) 1169–1180, http://dx.doi.org/10.1021/es0108077.

[23] S.G. Poulopoulos, D.P. Samaras, C.J. Philippopoulos, Atmos. Environ. 35 (26) (2001) 4399–4406, http://dx.doi.org/10.1016/S1352-2310(01)00248-5.

[24] B.-Q. He, S.-J. Shuai, J.-X. Wang, H. He, Atmos. Environ. 37 (35) (2003) 4965–4971, http://dx.doi.org/10.1016/j.atmosenv.2003.08.029.

[25] S. Machado Corrêa, G. Arbilla, Atmos. Environ. 42 (4) (2008) 769–775, http://dx.doi.org/10.1016/j.atmosenv.2007.09.073.

[26] T.M. Cahill, R.A. Okamoto, Environ. Sci. Technol. 46 (15) (2012) 8382–8388, http://dx.doi.org/10.1021/es301659u.

[27] R. Ballesteros, J.J. Hernández, J. Guillén-Flores, Fuel 95 (0) (2012) 136–145, http://dx.doi.org/10.1016/j.fuel.2011.09.012.

[28] E. Ranzi, M. Corbetta, F. Manenti, S. Pierucci, Chem. Eng. Sci. (0), doi: 10.1016/j.ces.2013.08.014.

[29] A.M. Dean, R.L. Johnson, D.C. Steiner, Combust. Flame 37 (0) (1980) 41–62, http://dx.doi.org/10.1016/0010-2180(80)90070-X.

[30] S. Hochgreb, F.L. Dryer, Combust. Flame 91 (3-4) (1992) 257–284, http://dx.doi.org/10.1016/0010-2180(92)90058-W.

[31] Y. Román-Leshkov, C.J. Barrett, Z.Y. Liu, J.A. Dumesic, Nature 447 (7147) (2007) 982–985.

[32] G. Friedrichs, D.F. Davidson, R.K. Hanson, Int. J. Chem. Kinet. 34 (6) (2002) 374–386, http://dx.doi.org/10.1002/kin.10059.

[33] B. Eiteneer, C.L. Yu, M. Goldenberg, M. Frenklach, J. Phys. Chem. A 102 (27) (1998) 5196–5205, http://dx.doi.org/10.1021/jp981184v.

[34] Y. Hidaka, T. Taniguchi, H. Tanaka, T. Kamesawa, K. Inami, H. Kawano, Combust. Flame 92 (4) (1993) 365–376, http://dx.doi.org/10.1016/0010-2180(93)90149-W.

[35] P. Glarborg, M.U. Alzueta, K. Kjærgaard, K. Dam-Johansen, Combust. Flame 132 (4) (2003) 629–638, http://dx.doi.org/10.1016/S0010-2180(02)00535-7.

[36] Y. Hidaka, T. Taniguchi, T. Kamesawa, H. Masaoka, K. Inami, H. Kawano, Int. J. Chem. Kinet. 25 (4) (1993) 305–322.

[37] A.M. Dean, R.L. Johnson, D.C. Steiner, Combust. Flame 37 (1980) 41–62.

[38] J. Li, Z. Zhao, A. Kazakov, M. Chaos, F.L. Dryer, J.J. Scire, Int. J. Chem. Kinet. 39 (3) (2007) 109–136, http://dx.doi.org/10.1002/kin.20218.

[39] M.P. Halstead, A. Prothero, C.P. Quinn, Proc. Roy. Soc. Lond. A. Math. Phys. Sci. 322 (1550) (1971) 377–403, http://dx.doi.org/10.1098/rspa.1971.0074.

[40] P. Gray, J.F. Griffiths, S.M. Hasko, P.-G. Lignola, Proc. Roy. Soc. Lond. A. Math. Phys. Sci. 374 (1758) (1981) 313–339, http://dx.doi.org/10.1098/rspa.1981.0025.

[41] J. Cavanagh, R.A. Cox, G. Olson, Combust. Flame 82 (1) (1990) 15–39, http://dx.doi.org/10.1016/0010-2180(90)90075-3.

[42] F.P. Di Maio, P.G. Lignola, P. Talarico, Combust. Sci. Technol. 91 (1–3) (1993) 119–142, http://dx.doi.org/10.1080/00102209308907636.

[43] E.W. Kaiser, C.K. Westbrook, W.J. Pitz, Int. J. Chem. Kinet. 18 (6) (1986) 655–688, http://dx.doi.org/10.1002/kin.550180606.

[44] P. Dagaut, M. Reuillon, D. Voisin, M. Cathonnet, M. McGuinness, J.M. Simmie, Combust. Sci. Technol. 107 (4–6) (1995) 301–316, http://dx.doi.org/10.1080/00102209508907809.

[45] Y. Hidaka, S. Kubo, T. Hoshikawa, H. Wakamatsu, in: Z. Jiang (Ed.), Shock Waves, Springer Berlin Heidelberg, 2005, pp. 603–608.

[46] K. Yasunaga, S. Kubo, H. Hoshikawa, T. Kamesawa, Y. Hidaka, Int. J. Chem. Kinet. 40 (2) (2008) 73–102, http://dx.doi.org/10.1002/kin.20294.

[47] G. da Silva, J.W. Bozzelli, J. Phys. Chem. A 110 (48) (2006) 13058–13067, http://dx.doi.org/10.1021/jp063772b.

[48] E.W. Kaiser, Int. J. Chem. Kinet. 19 (5) (1987) 457–486, http://dx.doi.org/10.1002/kin.550190506.

[49] A. Lifshitz, C. Tamburu, A. Suslensky, J. Phys. Chem. 94 (7) (1990) 2966–2972, http://dx.doi.org/10.1021/j100370a043.

[50] T. Kasper, U. Struckmeier, P. Oßwald, K. Kohse-Höinghaus, Proc. Combust. Inst. 32 (1) (2009) 1285–1292, http://dx.doi.org/10.1016/j.proci.2008.06.040.

[51] B. Akih-Kumgeh, J.M. Bergthorson, Combust. Flame 158 (10) (2011) 1877–1889, http://dx.doi.org/10.1016/j.combustflame.2011.02.015.

[52] P.S. Veloo, P. Dagaut, C. Togbe, G. Dayma, S.M. Sarathy, C.K. Westbrook, F.N. Egolfopoulos, Proc. Combust. Inst. 34 (1) (2013) 599–606, http://dx.doi.org/10.1016/j.proci.2012.06.138.

[53] P.S. Veloo, P. Dagaut, C. Togbé, G. Dayma, S.M. Sarathy, C.K. Westbrook, F.N. Egolfopoulos, Combust. Flame 160 (9) (2013) 1609–1626, http://dx.doi.org/10.1016/j.combustflame.2013.03.018.

[54] D. Davidson, S. Ranganath, K.-Y. Lam, M. Liaw, Z. Hong, J. Propul. Power 26 (2) (2010) 280–287.

[55] S. Dooley, H.J. Curran, J.M. Simmie, Combust. Flame 153 (1-2) (2008) 2–32, http://dx.doi.org/10.1016/j.combustflame.2008.01.005.

[56] J. Zhang, L. Pan, J. Mo, J. Gong, Z. Huang, C.K. Law, Combust. Flame 160 (9) (2013) 1541–1549, http://dx.doi.org/10.1016/j.combustflame.2013.04.002.

[57] J. Zhang, L. Pan, Z. Zhang, J. Mo, Z. Huang, Energy Fuels 27 (5) (2013) 2804–2810, http://dx.doi.org/10.1021/ef302164n.

[58] D. Healy, N. Donato, C. Aul, E. Petersen, C. Zinner, G. Bourque, H. Curran, Combust. Flame 157 (8) (2010) 1526–1539.

[59] D. Healy, D.M. Kalitan, C.J. Aul, E.L. Petersen, G. Bourque, H.J. Curran, Energy Fuels 24 (3) (2010) 1521–1528, http://dx.doi.org/10.1021/ef9011005.

[60] D. Healy, M.M. Kopp, N.L. Polley, E.L. Petersen, G. Bourque, H.J. Curran, Energy Fuels 24 (3) (2010) 1617–1627, http://dx.doi.org/10.1021/ef901292j.

[61] S. Burke. Development of a Chemical Kinetic Mechanism for Small Hydrocarbons. Ph.D. Thesis, National University of Ireland Galway, 2013.

[62] W.K. Metcalfe, S.M. Burke, S.S. Ahmed, H.J. Curran, Int. J. Chem. Kinet. 45 (10) (2013) 638–675, http://dx.doi.org/10.1002/kin.20802.

[63] A. Kéromnès, W.K. Metcalfe, K.A. Heufer, N. Donohoe, A.K. Das, C.-J. Sung, J. Herzler, C. Naumann, P. Griebel, O. Mathieu, M.C. Krejci, E.L. Petersen, W.J. Pitz, H.J. Curran, Combust. Flame 160 (6) (2013) 995–1011, http://dx.doi.org/10.1016/j.combustflame.2013.01.001.

[64] E. Ranzi, A. Frassoldati, R. Grana, A. Cuoci, T. Faravelli, A.P. Kelley, C.K. Law, Prog. Energy Combust. Sci. 38 (4) (2012) 468–501, http://dx.doi.org/10.1016/j.pecs.2012.03.004.

[65] Y. Hidaka, S. Shiba, H. Takuma, M. Suga, Int. J. Chem. Kinet. 17 (4) (1985) 441–453, http://dx.doi.org/10.1002/kin.550170410.

[66] Y. Hidaka, T. Nakamura, A. Miyauchi, T. Shiraishi, H. Kawano, Int. J. Chem. Kinet. 21 (8) (1989) 643–666, http://dx.doi.org/10.1002/kin.550210805.

[67] Y. Hidaka, K. Hattori, T. Okuno, K. Inami, T. Abe, T. Koike, Combust. Flame 107 (4) (1996) 401–417, http://dx.doi.org/10.1016/S0010-2180(96)00094-6.

[68] Y. Hidaka, K. Kimura, K. Hattori, T. Okuno, Combust. Flame 106 (1-2) (1996) 155–167, http://dx.doi.org/10.1016/0010-2180(95)00252-9.

[69] C. Morley Gaseq. <http://www.gaseq.co.uk>.

[70] K.P. Somers, J.M. Simmie, F. Gillespie, C. Conroy, G. Black, W.K. Metcalfe, F. Battin-Leclerc, P. Dirrenberger, O. Herbinet, P.-A. Glaude, Combust. Flame 160 (11) (2013) 2291–2318.

[71] J.M. Smith, J.M. Simmie, H.J. Curran, Int. J. Chem. Kinet. 37 (12) (2005) 728–736, http://dx.doi.org/10.1002/kin.20120.

[72] R. Hanson, D. Davidson, Progr. Energy Combust. Sci. (2014).

[73] E.R. Ritter, J.W. Bozzelli, Int. J. Chem. Kinet. 23 (9) (1991) 767–778, http://dx.doi.org/10.1002/kin.550230903.

[74] S.W. Benson, J.H. Buss, J. Chem. Phys. 29 (3) (1958) 546–572, http://dx.doi.org/10.1063/1.1744539.

[75] A.M. Dean, J. Phys. Chem. 89 (21) (1985) 4600–4608, http://dx.doi.org/10.1021/j100267a038.

[76] A. Chang, J. Bozzelli, A. Dean, Z. Phys. Chem. 214 (11/2000) (2000) 1533.

[77] L.S. Kassel, J. Phys. Chem. 32 (2) (1928) 225–242.

[78] M. Frisch, G. Trucks, H. Schlegel, G. Scuseria, M. Robb, J. Cheeseman, G. Scalmani, V. Barone, B. Mennucci, G. Petersson, in: Inc: 2009.

[79] A.D. Becke, J. Chem. Phys. 98 (7) (1993) 5648–5652.

[80] C. Lee, W. Yang, R. Parr, Phys. Rev. B 37 (2) (1988) 785–789, http://dx.doi.org/10.1103/PhysRevB.37.785.

[81] J. Zádor, A.W. Jasper, J.A. Miller, Phys. Chem. Chem. Phys. 11 (46) (2009) 11040–11053.

[82] P. Zhang, S.J. Klippenstein, C.K. Law, J. Phys. Chem. A 117 (9) (2013) 1890–1906.

[83] D.R. Lide, CRC Handbook of Chemistry and Physics, CRC Press, 2004. 1-523 of Section 3.

[84] R.J. Kee, M.E. Coltrin, P. Glarborg, Chemically Reacting Flow: Theory and Practice, John Wiley & Sons, 2005, pp. 496–499.

[85] J.R. Barker, Int. J. Chem. Kinet. 33 (4) (2001) 232–245.

[86] J.R. Barker, Int. J. Chem. Kinet. 41 (12) (2009) 748–763.

[87] M.A. Oehlschlaeger, D.F. Davidson, R.K. Hanson, Proc. Combust. Inst. 30 (1) (2005) 1119–1127.

[88] M.A. Oehlschlaeger, D.F. Davidson, R.K. Hanson, J. Phys. Chem. A 108 (19) (2004) 4247–4253.

[89] Z. Serinyel, N. Chaumeix, G. Black, J. Simmie, H. Curran, J. Phys. Chem. A 114 (46) (2010) 12176–12186.

[90] J.P. Orme, H.J. Curran, J.M. Simmie, J. Phys. Chem. A 110 (1) (2005) 114–131, http://dx.doi.org/10.1021/jp0543678.

[91] E. Ranzi, A. Sogaro, P. Gaffuri, G. Pennati, C.K. Westbrook, W.J. Pitz, Combust. Flame 99 (2) (1994) 201–211.

[92] J.M. Simmie, J. Phys. Chem. A 116 (18) (2012) 4528–4538, http://dx.doi.org/10.1021/jp301870w.

[93] H.J. Curran, Int. J. Chem. Kinet. 38 (4) (2006) 250–275, http://dx.doi.org/10.1002/kin.20153.

[94] L.K. Huynh, A. Violi, in: Ab Initio Study on the Methyl Butanoate Decomposition, The 2007 Annual Meeting, 2007, 2007.

[95] D.M. Matheu, W.H. Green, J.M. Grenda, Int. J. Chem. Kinet. 35 (3) (2003) 95–119, http://dx.doi.org/10.1002/kin.10106.
[96] M. Dente, G. Bozzano, T. Faravelli, A. Marongiu, S. Pierucci, E. Ranzi, in: B.M. Guy (Ed.), Advances in Chemical Engineering, vol. 32, Academic Press, 2007, pp. 51–166.
[97] H.J. Curran, P. Gaffuri, W.J. Pitz, C.K. Westbrook, Combust. Flame 114 (1–2) (1998) 149–177, http://dx.doi.org/10.1016/S0010-2180(97)00282-4.
[98] A. Cuoci, A. Frassoldati, T. Faravelli, E. Ranzi, in: Open SMOKE: Numerical Modeling of Reacting Systems with Detailed Kinetic Mechanisms, XXXIV Meeting of the Italian Section of the Combustion Institute, 2011, 2011.
[99] D. Manca, G. Buzzi-ferraris, T. Faravelli, E. Ranzi, Combust. Theor. Model. 5 (2) (2001) 185–199, http://dx.doi.org/10.1088/1364-7830/5/2/304.
[100] G. Buzzi-Ferraris, F. Manenti, Comput. Aid. Chem. Eng. 30 (2) (2012) 1312–1316.
[101] C.-W. Zhou, J.M. Simmie, H.J. Curran, Phys. Chem. Chem. Phys. 13 (23) (2011) 11175–11192.
[102] J. Mendes, C.-W. Zhou, H.J. Curran, J. Phys. Chem. A 117 (22) (2013) 4515–4525, http://dx.doi.org/10.1021/jp4000413.
[103] S. Wang, D.F. Davidson, R.K. Hanson, Proc. Combust. Inst. (2014) (in press). doi: 10.1016/j.proci.2014.06.112.
[104] E. Ranzi, M. Dente, T. Faravelli, G. Pennati, Combust. Sci. Technol. 95 (1–6) (1993) 1–50.
[105] E. Ranzi, M. Dente, A. Goldaniga, G. Bozzano, T. Faravelli, Prog. Energy Combust. Sci. 27 (1) (2001) 99–139.
[106] R.J. Kee, F.M. Rupley, J.A. Miller, in: Sandia National Labs., Livermore, CA (USA): 1989.
[107] A. Burcat, B. Ruscic, Chemistry, T.-I. I. o. Tech., in: 2005, p Medium: ED.
[108] C.V. Naik, K.V. Puduppakkam, E. Meeks, J. Eng. Gas Turb. Power 134 (2) (2012).